PULSED LASER DEPOSITION OF TiO$_2$ THIN FILMS

TiO$_2$ ÕHUKESTE KILEDE SADESTAMINE LASERABLATSIOONI MEETODIL

MASTER THESIS

Student:	Andrus Vaarik
Student code:	204674
Supervisor:	Maris Pilvet, PhD, researcher
	Sergei Bereznev, PhD, Associate Professor

Tallinn 2023

(*On the reverse side of title page*)

AUTHOR'S DECLARATION

Hereby I declare, that I have written this thesis independently.

No academic degree has been applied for based on this material. All works, major viewpoints and data of the other authors used in this thesis have been referenced.

"11" January 2023.

Author: ....

/signature /

Thesis is in accordance with terms and requirements

"11" January 2023.

Supervisor: …..........................

/signature/

Accepted for defence

"......."....................2023 .

Chairman of theses defence commission: ....

/name and signature/

Non-exclusive licence for reproduction and publication of a graduation thesis[1]

I Andrus Vaarik

1. grant Tallinn University of Technology free licence (non-exclusive licence) for my thesis

PULSED LASER DEPOSITION OF TiO_2 THIN FILMS,

supervised by Maris Pilvet and Sergei Bereznev.

1.1 to be reproduced for the purposes of preservation and electronic publication of the graduation thesis, incl. to be entered in the digital collection of the library of Tallinn University of Technology until expiry of the term of copyright;

1.2 to be published via the web of Tallinn University of Technology, incl. to be entered in the digital collection of the library of Tallinn University of Technology until expiry of the term of copyright.

2. I am aware that the author also retains the rights specified in clause 1 of the non-exclusive licence.

3. I confirm that granting the non-exclusive licence does not infringe other persons' intellectual property rights, the rights arising from the Personal Data Protection Act or rights arising from other legislation.

11.01.2023

---

[1] *The non-exclusive licence is not valid during the validity of access restriction indicated in the student's application for restriction on access to the graduation thesis that has been signed by the school's dean, except in case of the university's right to reproduce the thesis for preservation purposes only. If a graduation thesis is based on the joint creative activity of two or more persons and the co-author(s) has/have not granted, by the set deadline, the student defending his/her graduation thesis consent to reproduce and publish the graduation thesis in compliance with clauses 1.1 and 1.2 of the non-exclusive licence, the non-exclusive license shall not be valid for the period.*

<div align="center">

Department of Materials and Environmental Technology

THESIS TASK

</div>

Student: Andrus Vaarik, 204674(name, student code)

Study programme: KAYM09/18 Materials and Processes for Sustainable Energetics

Main speciality: materials for sustainable energetics

Supervisor(s):Maris Pilvet, PhD, Researcher, +372 6203362

Sergei Bereznev, PhD, Associate Professor

Thesis topic:

(in English)   *PULSED LASER DEPOSITION OF TiO$_2$ THIN FILMS*

(in Estonian)   TiO2 ÕHUKESTE KILEDE SADESTAMINE LASERABLATSIOONI MEETODIL

Thesis main objectives:

1. To familiarise with the PLD deposition method and fabrication of monograin layer solar cells.

2. To investigate the properties of the deposited TiO$_2$ thin films.

3. To investigate the influence of the deposited TiO$_2$ thin films on the output parameters of the monograin layer solar cells

Thesis tasks and time schedule:

No	Task description	Deadline
1.	PLD depositions of TiO$_2$ thin films.	
2.	Characterization of the deposited TiO$_2$ thin films.	
3.	Characterization of the monograin layer solar cells.	

Language: English **Deadline for submission of thesis:** "12" January 2023.a

Student: Andrus Vaarik   .....……....... "11" January 2023.a

Supervisor: Maris Pilvet   ……………………..   "11" January 2023.a

Co-supervisor: Sergei Bereznev …......................   "11" January 2023.a

Head of study programme: ……………   .... "......."......................2023.a

<div align="center">

/signature/

</div>

Terms of thesis closed defence and/or restricted access conditions to be formulated on the reverse side

CONTENTS

6

PREFACE

The making of the following thesis was proposed by Dr. Maris Pilvet, who also became my supervisor, when I approached her with my desire to write the thesis in the Laboratory of Photovoltaic Materials. During the work I was consistently helped by many of the workers of both Laboratory of Photovoltaic Materials, namely Dr. Sergei Bereznev, the co-supervisor, Dr. Olga Volobujeva, Dr. Mati Danilson, Dr. Reelika Kaupmees, Dr. Valdek Mikli, Dr. Peter Robert Walke.

The most amount of help came from, and a special thanks go to my supervisor Dr. Maris Pilvet, without who I could not have finished this work. She went above and beyond to make sure that I will complete this thesis by proposing different viewpoints of the results, helping me with both the tests and research, giving me confidence, when I was not sure in continuing and educating me when my knowledge was lacking, despite me not always being timely with the work due to my own faults.

Keywords: Pulsed laser deposition, TiO_2, CZTS, thin film solar cells, monograin layer solar cells

List of abbreviations and symbols

AFM   Atomic force microscope

ALD   Atomic layer deposition

AM 1.5   A standard spectrum for solar cell testing

AZO   Aluminum doped ZnO, ZnO:Al

CBO   Conduction band offset

CIGS   Copper-Indium-Gallium-Selenide, $Cu(In,Ga)Se_2$

CZTS   Copper-Zinc-Tin-Sulfide, Cu_2ZnSnS_4

E_C Conduction band energy level

EDS   Energy dispersive x-ray analysis

E_F Fermi energy level

E_G Band gap energy

E_V Valence band energy level

FF   Fill factor

I_{Ph} light generated current

I_{SC} Short-circuit current

J_{SC} Short-circuit current density

k Boltzmann constant - $8.617385 \cdot 10^{-5}$ eV/K

MGL   Monograin layer

n-type   Semiconductor with electrons as majority charge carrier

PLD   Pulsed laser deposition

P_{light} Intensity of light for AM 1.5 - 100 mW/cm^2

P_{MPP} Power of solar cell at maximum power point

p-type   Semiconductor with holes as majority charge carrier

q Elementary charge

R_S Series resistance

R_{Sh} Shunt resistance

SEM   Scanning electron microscope

T Temperature

V_{bi} Built-in voltage

V_{OC} Open-circuit voltage

XPS   X-ray photoelectron spectroscopy

η Efficiency of solar cell

1. INTRODUCTION

The need for renewable energy technologies is becoming increasingly obvious with the recent crises the world has recently seen. In addition to the negative environmental effect of fossil fuels, the potential of losing energy sources due to simply being cut from them for political has become a real threat. This in turn has led to high prices of the fossil fuels, affecting everyone with increased energy prices, as about 80% of global population lives in countries that are net energy importers [1].

With the abundance of renewable energy, which has not yet been harnessed, the potential to increase the energy independence of countries world-wide exists. Having a de-centralized energy system with prices not affected so much by the highly varying fossil fuel prices, could be a future reality [1].

Among the renewable energy sources, global average cost of electricity from photovoltaic projects has fallen 85% from the year 2010 to 2020, the most from any renewable source [1]. Despite this, in recent years the annual photovoltaic additions are not on track (126 GW/year vs. needed 444 GW/year) to achieve the target of reducing global warming to only 1.5°C by 2050 [1].

Although most commercial solar technologies are based on silicon, thin film solar cells (based on CdTe and CIGS (Cu(In,Ga)Se$_2$)) allows for an inherently higher efficiency. Another benefit of thin film solar cells is that they can be implemented into flexible and lightweight structures, allowing for more de-centralized power by integration with buildings, devices, vehicles, etc. The drawback of the CdTe and CIGS solar cells are the requirement of expensive elements in their composition (In, Ga) and the toxicity of Cd [2]. Other thin film solar cell technologies have been less successful, due to not being as mature in regards of development. Among them is the kesterite based solar cell CZTS (Cu$_2$ZnSnS$_4$), which is also incorporated in this work.

A major challenge of the CZTS solar cells is the deficiency of the open-circuit voltage, which is in part attributed to interface recombinations at its p-n junction[3]–[7]. Many solutions have been tried with minor success. One proposed solution has been to implement a TiO$_2$ layer within the structure of the solar cell, acting as a barrier for the interface recombinations [7], [8].

In this work pulsed laser deposition (PLD) of TiO$_2$ was carried out as a preliminary trial of characterising the obtained thin film and seeing its effect on the CZTS based monograin layer solar cell, when incorporated in the solar cell structure.

In the following thesis work an overview of the basis of solar cell work is given and different solar cell technologies are briefly introduced. Following that, the deficiency of open-circuit voltage has been delved into more deeply and some trial solutions and their success are described. The TiO_2 properties and deposition methods are further introduced following with a brief introduction of the PLD process. In the experimental part the monograin layer technology preparation and the characterization methods used in the work are introduced. The results of the characterization of both the thin film and the solar cells achieved is discussed in the fourth part of the thesis.

2. LITERATURE OVERVIEW

2.1 Working principle of solar cells

2.1.1 Semiconductors, band gaps and doping

Almost all solar cell technologies are based on semiconductors. Semiconductors are materials that act as conductors in some condition but can also act as insulators in some other conditions. Notably the conductivity of a semiconductor rises with temperature increase. This is because at every temperature above absolute zero, some electrons of a semiconductor material have enough energy to "escape" their bonds with the atoms and are free to move around and in the presence of an electric field, can participate in conducting electricity. The higher the temperature, the more of these electrons can participate in conducting electricity [9], [10].

Due to Pauli exclusion principle the bonded electrons cannot have the same energy level. They form an energy band - each electron has a slightly different energy than all other ones. This energy band is called the valence band – called so because the electrons that form the bonds between atoms are called the valence electrons. If a bonded electron receives enough energy to be freed from the bond, then in the higher energy state it still has to abide by the Pauli exclusion principle. Electrons in the higher energy state also form a band – the conduction band. The name band gap comes from the energy state "gap" in which the electrons cannot exist [9], [10].

The energy that is necessary for the electron to break free of the bond is called the band gap energy. In other words, when the electron gains the energy necessary to break free of the bond it will be at a higher energy level, as the free electron, than it was when it was bonded. The band gap energy is the minimum energy required for the electron to reach this higher energy level [9], [10]. This has been illustrated in Figure 1.
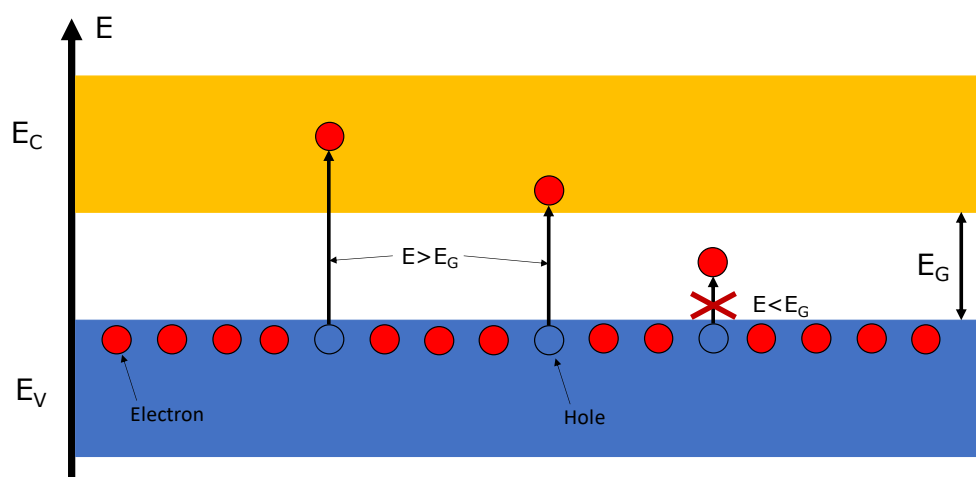
Figure 1 Illustration of the band gap. E_C signifies the conduction band energy level, E_V the valence band energy level and E_G the band gap energy.

In a semiconductor with no crystallographic defects or dopants all the electrons take part in a bond. But if a different atom is introduced into the material, which has a larger or smaller amount of valence electrons that the atom it replaces, an extra electron or a deficiency of an electron (hole) is introduced into the material. The extra carrier is bound to the atom with smaller energy than the other valence electrons. In the band diagram this is seen as small extra energy levels in the band gap. This introduction of a foreign atom is called doping. Introducing a dopant with an extra valence electron is called ntype doping and introducing a dopant with a missing valence electron is called p-type doping. The n-type doping introduces an energy level near the bottom of the conduction band, p-type doping introduces an energy level near the top of the valence band. [9]

2.1.2 p-n junction

The underlying working principle of most solar cells - and definitely the commercially available solar cells is based on the p-n junction of semiconductors. The p-n junction is formed when two semiconductor materials, one with excess of electrons (n-type) and one with excess of holes (p-type), are joined. Joining of the materials allows the majority carriers from either material to diffuse into the other. This diffusion however leaves behind the exposed charges of the atoms to which the electrons or holes originally belonged to. These atoms are fixed in the crystal lattice and cannot move. In the n-type material positive ion cores are exposed and, in the p-type material negative ion cores are exposed. Between these ion cores an electric field is formed. In this region (depletion region) near the contact area of the two semiconductors, the free carriers are quickly moved out due to the electric field – the region is depleted of free carriers [9], [10].

Another way of looking at the p-n junction formation is in the form of the band alignment. The simplest explanation for the band alignment can be done through the Fermi energy level, E_F. The Fermi energy level is defined as the energy level of which's occupation probability is 50%. In other words, at a given temperature (>0K) some electrons in a semiconductor are always excited to the conduction band – this means that the average energy level of all valence electrons in the semiconductor is higher than the valence band energy level. Therefore, the theoretical probability of an electron occupying an energy level in the band gap increases [9].

Going back to the doping discussion, in an n-doped semiconductor additional energy levels are introduced near the conduction band and electrons from those additional levels easily transition to the conduction band, therefore the average energy level of electrons in the material increases – Fermi level is shifted towards the conduction band when compared to a non-doped semiconductor of the same type. The opposite is true for the p-doped semiconductor [9].

When the n- and p-type semiconductors are brought together, their Fermi energy levels must be the same if the system is in thermal equilibrium. Practically this is the effect of the diffusion current discussed earlier – electrons flow from the n-type material to the p-type to fill the holes. The alignment of the Fermi energy levels is the cause of the band bending [9]. Band bending can be seen in Figure 2.
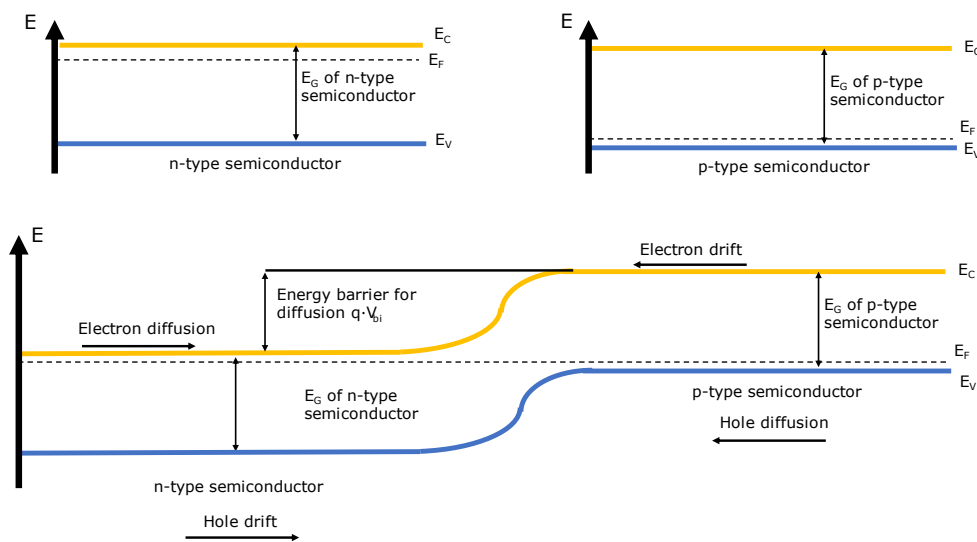

Figure 2 Band bending and fermi level alignment of n- and p-type semiconductor upon their connection. q signifies the electronic charge and V_{bi} the built-in voltage of the p-n junction.

In the junction there are two different forces affecting the charge carriers. Both the holes and electrons are affected by the diffusion, holes are diffusing from the p-type to

the n-type semiconductor. Both the holes and electrons are also affected by the built-in electric field, which is making the electrons flow back to the n-type semiconductor and holes to the p-type semiconductor. When no external voltage is applied to the device, the net current is zero, meaning the diffusion and drift currents balance each other [9], [10].

If a forward bias is applied to the p-n junction, meaning a positive voltage is applied to the p-type material and negative to the n-type, a current flow is observed. The forward bias increases the diffusion current, by decreasing the built-in electric field in the p-n junction, as the applied electric field is the opposite of the built-in field [9], [10].

A reverse bias the voltage is applied across the device in the opposite direction to the forward bias, meaning negative voltage to p-type material and positive to n-type. The reverse bias increases the built-in voltage in the depletion area. Larger electric field in the depletion area means that it is more difficult for carriers to diffuse across it [9], [10].

2.1.3 Light generated current

Light generated current consists of two processes. First a photon is absorbed, and electron-hole pair is generated. This alone is not enough, because in a p-type material, the electrons are minority carriers and recombine very quickly. The same applies to the holes in an n-type semiconductor. If the recombination happens, then the energy is lost [9], [10].

The second key process of light generated current is the carrier separation. This process is facilitated by the p-n junction's built-in electric field. If the light generated minority carrier is close enough to the depletion zone it will be moved to the other side of the junction by the electric field, where it becomes a majority carrier, the drift current increases [9], [10].

Now the light generated carriers are separated and if the solar cell's contacts are short-circuited, they will recombine – the current will flow, this is known as the short-circuit current I_{sc}. If, however the contacts are separated from each other, then the electrons and holes have nowhere to flow, the diffusion current will rise because of larger concentration of electrons in the n-type material and larger concentration of holes in the p-type material. The larger majority charge carrier concentration will also create a new, opposing electric field to the p-n junction's electric field, because both the p-type material and n-type material will have a charge, separated by the p-n junction. The larger the majority carrier concentration difference, the larger the new electric field

strength. This new electric field also increases to the diffusion current. The diffusion current and drift current will reach a balance again. The contacts will have a potential difference between them because of the larger concentration of electrons in the n-type material and larger concentration of holes in the p-type material. This potential difference is called the open circuit voltage V_{oc} [9], [10].

2.2 Solar cell technologies

2.2.1 First generation technologies

Solar cell technologies are most often divided into three generations based on the time since their emergence period. The first-generation technologies are all silicon based and are still the most efficient commercially available solar cells. The silicon based solar cells have many advantages. For example, silicon as a semiconductor can be doped to achieve an n-type (dopant P) semiconductor and also a p-type (dopant B) semiconductor. The technology is the most well developed, process of creating a good quality solar cell is quite well researched and understood. [2]. A disadvantage is of silicon based solar cells require very pure Silicon and purifying takes a lot of energy. In addition – higher efficiency solar cells are made of monocrystalline silicon, which requires even more energy. Record efficiency of a monocrystalline Si solar cell without a concentrator is 26,2% (Figure 3).
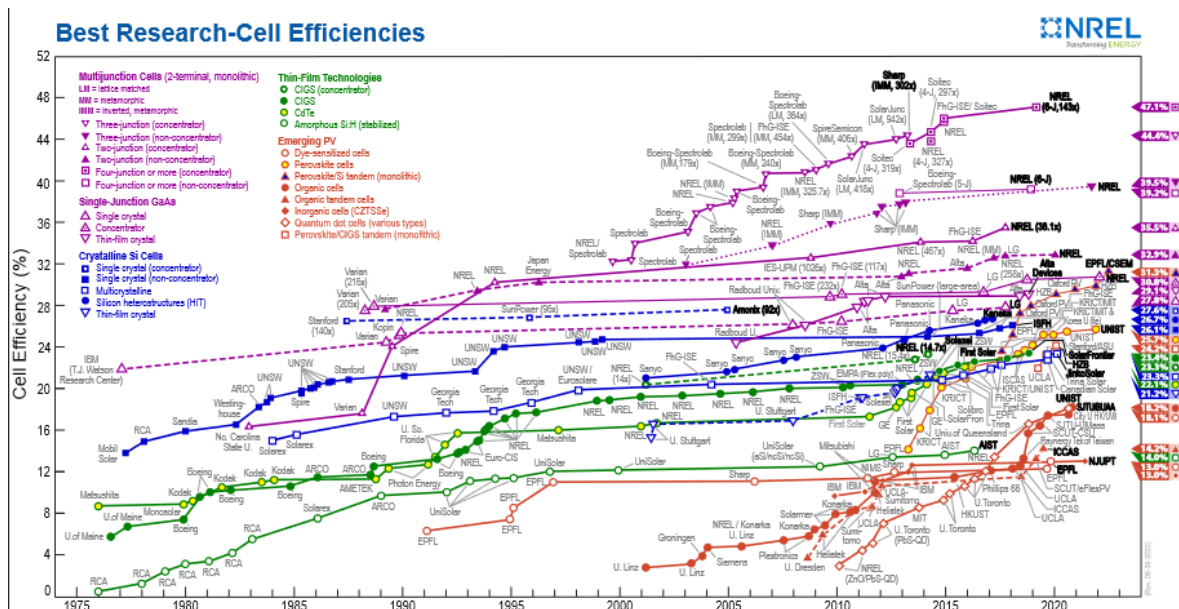

Figure 3 Best research-cell efficiencies [11].

2.2.2 Second generation technologies

Solar cells based on second generation technologies are also called thin-film solar cells because when compared to first generation solar cells the thickness of the cells is much smaller, usually made of layers only a few micrometers thick. Some thin-film solar cells could potentially provide lower cost energy than c-Si based solar cells. Most common thin-film solar cells are amorphous silicon based, Cadmium Telluride based, and Copper-Indium-Selenide (CIS) or Copper-Indium-Gallium-Selenide (CIGS) based. The difference of amorphous silicon and the first generation based solar cells is that the amorphous silicon is deposited on a substrate instead of growing the silicon crystals and then doping them. This makes it possible to have a very thin and flexible silicon layer. The downside is that the solar cells efficiency is much lower - record 14% [11]. Thin film solar cells also rely on the p-n junction to work. Thin film solar cells often consist of two different material layers to form the junction. The top layer is often a wider band gap material, which absorbs higher energy photons only. The bottom layer is called the absorber layer, made of smaller band gap material. It absorbs also the lower energy photons, which passed the wider band gap top layer. This design is in principle more efficient than the first-generation solar cells based on one material. Highest efficiency second generation solar cells are based on GaAs – reaching the record efficiency of 29.1% [11]. CIGS based cells have a record efficiency of 23.4% and CdTe 22.1%. The main problem of CIGS and GaAs based cells is that both indium and gallium are increasingly rare and expensive. Main problem of CdTe cells is that cadmium is a highly toxic material [2].

2.2.3 Third generation technologies

The third-generation technologies emerged due to the limited availability of materials and high toxicity of the second-generation solar cells and the high costs of first generation solar cells. A large difference of the third solar cell generation is that many of them do not rely on the p-n junction to work (Perovskite, Dye-Sensitized solar cells, quantum dot solar cells).

An exception to this are the kesterite Cu_2ZnSnS_4 (CZTS) or $Cu_2ZnSnSe_4$ (CZTSe) or $Cu_2ZnSn(SSe)_4$ (CZTSSe) solar cells. They still work based on the p-n junction. The kesterite solar cells are highly similar to the CIGS solar cells. The structure of the cells is similar and many of the technologies have been used in CZTS based solar cell structure as in the CIGS cell structures. The advantage of the kesterite cell in comparison with the CIGS cell is that it contains much more abundant elements. The kesterite based solar cells are also the ones investigated in this thesis.

They consist of comparatively abundant elements, have high absorption coefficients (10^{-4}–10^{-5} cm^{-1}), high hole concentration (10^{15} to 10^{20} cm^{-3}), giving it a p-type conductivity – mainly attributed to the Cu_{Zn} antisites in the crystal [13], and a suitable band gap of 0.9 (CZTSe) to ~1.4-1.5 (CZTS) eV. The record power conversion efficiency of a kesterite solar cell is currently 14.1% [14], which is yet too low for commercial applications [12]. There are many theories and proposals for increasing the efficiency of kesterite solar cells but the main challenge is decreasing the voltage loss due to interface recombination [3], [5]–[7].

2.2.4 Solar cell parameters

Before a more thorough understanding of the main problem of the thesis can be explained, it is necessary to know the principal solar cell parameters.

The characteristic IV curve

The IV curve is the current and voltage across the solar cell diode plotted on a graph (Figure 4). For each value of voltage, a corresponding value of current can be seen. In the dark the solar cell produces a normal diode IV-curve, which means the current is zero until a high enough voltage in the forward bias is reached, which allows the charge carriers to cross the depletion zone at which point the current value starts rising rapidly. If the solar cell is illuminated, the IV-curve is shifted by the amount of current that is generated by the light. At zero voltage, the value of current is the value of the short-circuit current I_{sc} mentioned before. And at zero current, the voltage value is the open-circuit voltage V_{oc} value mentioned before. The IV curve values of the light illuminated solar cell are often plotted in reverse, so the current values would be positive. The characteristic curve also describes the ohmic losses and leak currents in the solar cell and can be described by the characteristic curve equation:

$$I = I_{Ph} - I_0 \cdot \left(e^{\frac{q(V+I \cdot R_S)}{nkT}} - 1 \right) - \frac{V + I \cdot R_S}{R_{Sh}}$$

Equation 2.1

Where: I - measured current (A)
I_{Ph} – light generated current (A)
I_0 – saturation current (A)
q – elementary charge (A·s)
V – voltage value (V)
R_S – series resistance (Ω)
n – ideality factor
k – Boltzmann constant (W·s/K)

T – temperature (K)
R_{Sh} – shunt resistance (Ω)

Short-circuit current - I_{sc}

The short-circuit current is the current through the solar cell when the voltage across it is zero. Without accounting for losses to resistances the short-circuit current equals the light generated current. Graphically (Figure 4) the value of the short-circuit current can be seen as where the IV-curve intersects the current (y) axis. The value of I_{sc} depends on many different factors:

- The area of the solar cell – which is why usually the short-circuit current density is used, the current value is divided by the solar cell's area - J_{sc} (mA/cm^2).

- The light intensity, meaning the number of photons hitting the solar cell. Most often an intensity of 1000W/m^2 is used.

- The spectrum of the incident light. The intensity and spectrum are usually accounted for by using the AM1.5 spectrum.

- Optical properties of the solar cell – namely absorption of light and reflection of light.

- The probability of the minority carrier collection, which relies mostly on minority carrier lifetime in the corresponding material.

The short-circuit current's theoretical maximum value is determined by the band gap of the absorber material. In an ideal device, every photon which has an energy larger than the band gap value is converted into a charge carrier. In theory this means that the lowest band gap material has the highest short-circuit current.

In the cases of very high series resistance of the solar cell, the short circuit current value also decreases. Therefore, having a low series resistance is beneficial when trying to achieve a high efficiency solar cell. Often the short-circuit current is assumed to be equal to the illumination current. This is only the case if the series resistance of the solar cell is not too high.

Open-circuit voltage - V_{oc}

As mentioned before, the open-circuit voltage is the voltage that can be measured across the solar cell's contacts when no current is flowing, while the cell is illuminated. The separation of charge by the built-in electric field creates the voltage. As also

mentioned before, this larger concentration of majority carriers on each side of the p-n junction also increases the diffusion current, which is opposite to the drift current. When the diffusion current increases, it also increases the recombination of charge carriers. The recombination of charge carriers limits the open-circuit voltage that a solar cell can reach. The measure of charge carrier recombination is called the "dark saturation current" I_0.

The theoretical maximum short-circuit current increased when the band gap of the absorber material decreased. For the open-circuit voltage the opposite is true. In theory the amount of energy of the light generated electron-hole pair that can be extracted is the band gap energy. If the electron is excited beyond the band gap energy, then it quickly dissipates the extra energy as thermal energy and the energy that is left to be extracted is the band gap energy. Graphically the V_{OC} can be determined by the value where the IV-curve intersects the voltage (x) axis (Figure 4).

Fill factor - *FF*

At either point of operation – the short-circuit or open-circuit, no power is extracted from the solar cell. The fill factor is the ratio of maximum power of the solar cell (Figure 4, P_MPP) divided by the theoretical power of multiplying the V_{oc} and I_{sc} of the solar cell:

$$FF = \frac{P_{MPP}}{V_{OC} \cdot I_{SC}}$$

Equation 2.2

Efficiency – *η*

The efficiency of a solar cell is defined by the power generated by the solar cell divided by the input power (*P_light*) – usually 1000 W/m^2:

$$\eta = \frac{P_{MPP}}{P_{light}} \cdot 100\%$$
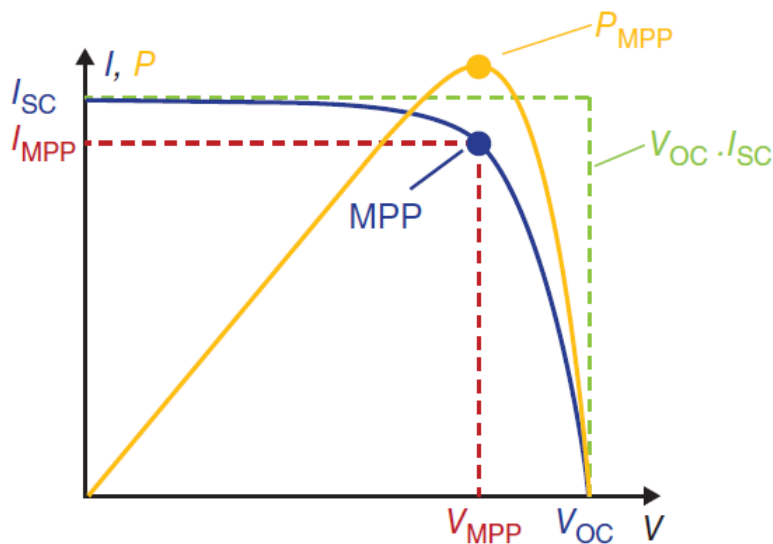
Equation 2.3

Figure 4 The current-voltage plot. Blue line signifies the real relation of current and voltage [9].

2.2.5 V_{OC} deficiency of kesterite solar cells

As briefly mentioned before a big challenge in increasing the efficiency of kesterite solar cells is increasing the open-circuit voltage [5]–[7], [15]–[17]. The loss in the V_{OC} of kesterite solar cells is mostly attributed to the recombination of charge carriers both in the bulk material [3], [16], [17], and the interface between the kesterite absorber layer and the buffer layer [3]–[7].

In most common contemporary CZTS, CZTSe or CZTSSe solar cells CdS is used as a buffer layer. In kesterite solar cells the absorber material is the kesterite, and CdS is the material that helps form the p-n junction, necessary for the solar cell to work. Kesterites are a p-type semiconductor and CdS is an n-type semiconductor.

The "cliff-like" conduction band offset (Figure 5 (a)) and low-quality p-n junction at the CZTS and CdS (buffer) interface lower the open circuit voltage (V_{OC}) of the photovoltaic device [3]. Both "cliff-like" [18],[19] and "spike-like" [20] conduction band offsets (Figure 5 (b)) have been reported at the CZTS-CdS junction. This discrepancy may be due to different processing methods, conditions, or treatments before the CdS deposition. It has been reported that a "cliff-like" conformation of conduction band offset significantly contributes to recombination of charge carriers at the interface. Conversely a "spike-like" conduction band offset prohibits this kind of recombination [7], [21].

It must be kept in mind that the "spike-like" conduction band offset should not be too large, as then it will create a barrier for the photogenerated carriers and leads to significant loss of charge carriers [22].
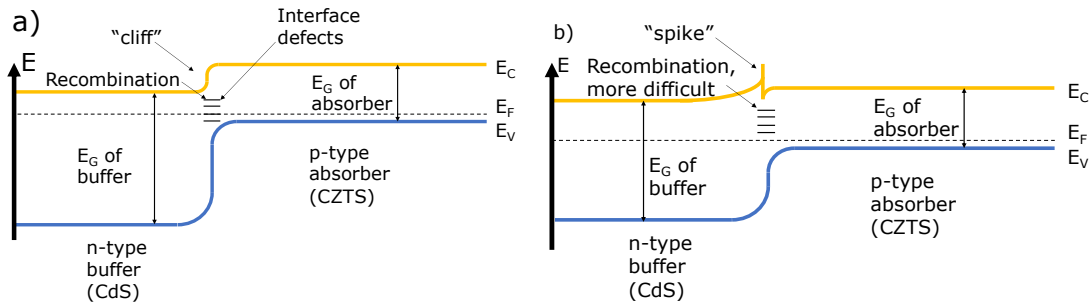
Figure 5 A "cliff" (a) and "spike" (b) like conduction band offsets of a p-n junction.

2.2.6 Proposed solutions

Following this idea of creating a "spike-like" conduction band offset in the solar cell structure between the absorber and buffer layer, different methods have been tried to achieve this situation. Slight thermal treatment (10 minutes at 200° C) of CZTSe/CdS thin film improved the devices V_{oc} slightly (4.5%) [23]. It has also been proposed to dope CZTS with Ag, near the p-n junction region. As the Cu_{Zn} antisites, which give the material the p-type conductivity, also play a role in recombination of charge carriers. Doping the decreases these defects in the doping region. Significant increase of V_{oc} has been seen with this method [24]–[26] . Trials have also been made to incorporate an alternative buffer layer or an intermediate material layer between the buffer and absorber, to produce a "spike-like" conduction band offset. A 100 mV increase to V_{oc} and a CBO of 0.37 eV was seen, when CdS buffer layer was replaced by a $Zn_{0.35}Cd_{0.65}S$ buffer layer [4]. A double buffer layer of ZnSnO/CdS has also been tried out, resulting in a 150 mV increase in V_{oc}, but also a large increase of series resistance of the cell [27]. In another study a V_{oc} increase from 638 mV to 657 mV was observed when an ultrathin (1.2 nm) SnO_2 layer was deposited by successive ionic layer adsorption and reaction method. The increase in Voc was also attributed to the theorized "spike-like" conduction band offset [28]. TiO_2 as an intermediate electron transport layer or an alternative buffer layer altogether has also been proposed [7], [8]. This in turn induces a "spike-like" configuration (Figure 6) of the conduction band offset [7].
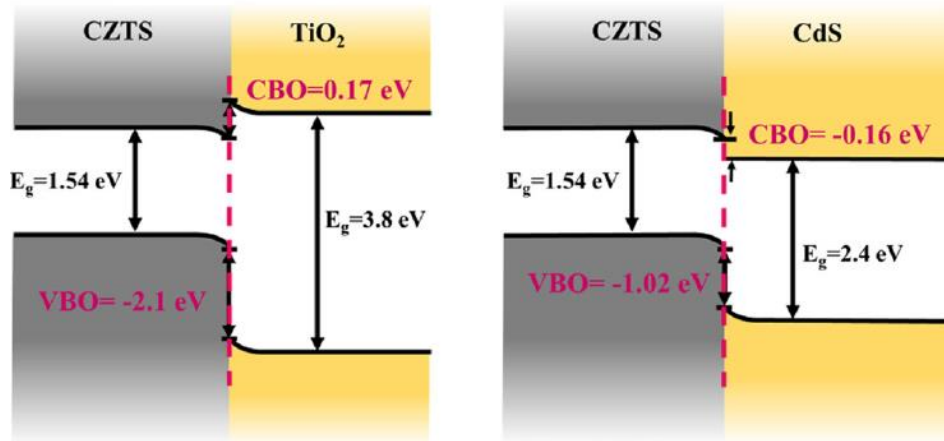
Figure 6 Schematic representation of the band alignment at the CZTS/TiO$_2$ and CZTS/CdS interfaces [7].

In this work the TiO$_2$ thin film layer was deposited in three different positions in the solar cell structure: before the CdS buffer layer, instead the buffer layer and after the buffer layer (instead of the *i*-ZnO layer, introduced below). These different trials were done to further investigate the possibilities of incorporating the TiO$_2$ thin layer in the monograin layer kesterite solar cell structure. The structure of CZTS/TiO$_2$/CdS/*i*-ZnO/AZO is tried to reduce the majority carrier recombination across the p-n junction as previously shown. The structure of CZTS/CdS/TiO$_2$/AZO is tried as the substitute of *i*-ZnO, in which the TiO$_2$ would act as a high resistance interlayer to prohibit shunting, effectively also acting as a layer prohibiting recombination, but the p-n junction of CZTS/CdS would still stay the same. And the last structure of CZTS/TiO$_2$/*i*-ZnO/AZO is also tried to see if a p-n junction of CZTS/TiO$_2$ could yield a beneficial effect. The illustrations of the theoretical band alignments for these solar cell structures can be seen below on Figure 7.
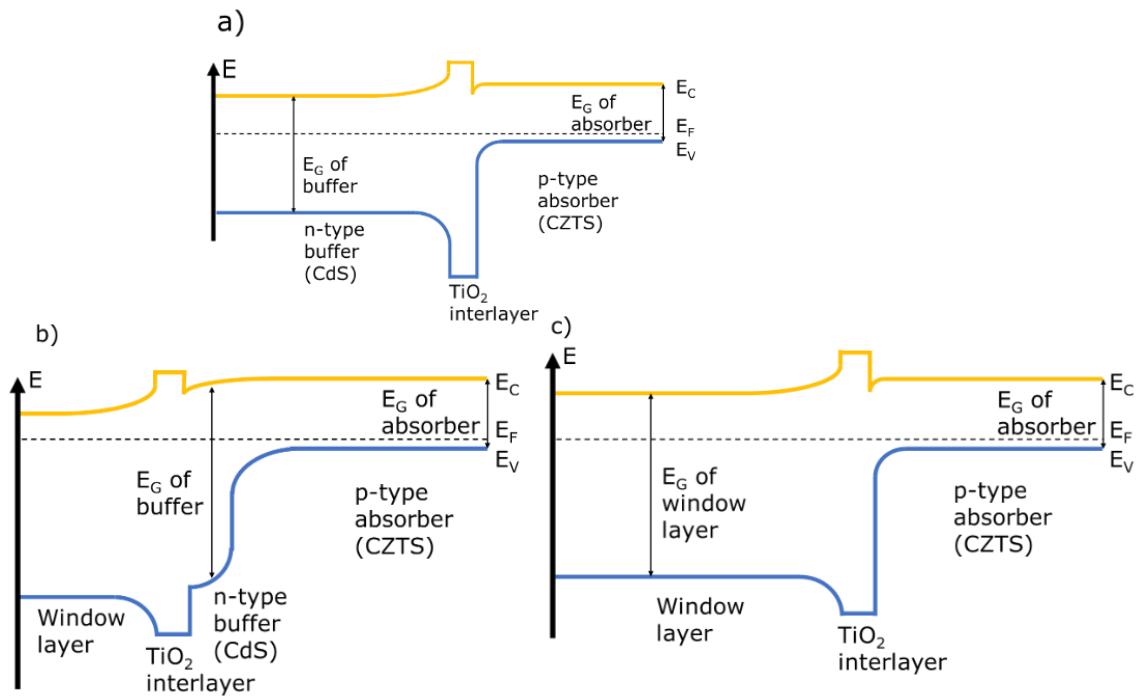
Figure 7 Illustrations of the theoretical band alignments of the solar cell structure with a) TiO_2 before the CdS, b) TiO_2 after the CdS, c) TiO_2 instead of the CdS.

2.3 TiO$_2$ properties

Titanium dioxide, titanium (IV) oxide or titania is an n-type semiconducting metal oxide. It has a wide range of applications both simple and high-tech. Common applications of titania include as white pigment in paint and toothpaste. Titanium oxide is also used in sunscreen as ultra-violet light blocking agent. TiO_2 is used due to its great optical and electrical properties in antireflection coatings, electrochromic devices, dye-sensitized solar cells, ultra-thin capacitors, photocatalysts and etc [29].

2.3.1 Crystal structures of TiO$_2$

In nature TiO_2 most commonly exists in three different polymorphs: anatase, brookite and rutile. All three polymorphs consist of TiO_6 octahedral units, differing in the distortion of the octahedral units and in edge and corner sharing [30]. The rutile phase (Figure 8, b) is the most thermodynamically favourable among the different structures and is the most densely packed (4.13 g/cm^3) [31]. In general, the rutile crystal structure is formed at temperatures greater than 800°C, although rutile phase has been achieved at lower temperatures (<450°C) by ion-assisted deposition or reactive evaporation [29]. Rutile TiO_2 has a tetragonal unit cell with the unit cell parameters of a = b = 4.585 Å and c = 2.953 Å [31].

The anatase phase (Figure 8, a) of TiO_2 like the rutile is a tetragonal crystal structure. It is a metastable phase of TiO_2, which transforms into the rutile phase at elevated temperatures [29]. The anatase phase has a unit cell with parameters of a = b = 3.784 Å and c = 9.515 Å.

The brookite (Figure 8, c) is the least common of the three naturally occurring TiO_2 polymorphs. Unlike anatase and rutile phases, brookite has an orthorhombic crystal structure, not tetragonal. The unit cell parameters of brookite are a = 9.184 Å, b = 5.447 Å and c = 5.154 Å [31].

The TiO_2 amorphous phase (am-TiO_2) (Figure 8, d) is most described as the partial loss of octahedral coordination and the under- and over-coordinated Ti ions. According to simulations, the electronic structure of am-TiO_2 is similar to the anatase phase [32]. Amorphous materials are thermodynamically metastable phases, so in some conditions they can evolve into the thermodynamically favourable (crystalline) phases. Common strategy to achieve crystalline phases from amorphous is to heat the amorphous material [30]. At 300°C the amorphous phase transitions to the anatase phase [33].
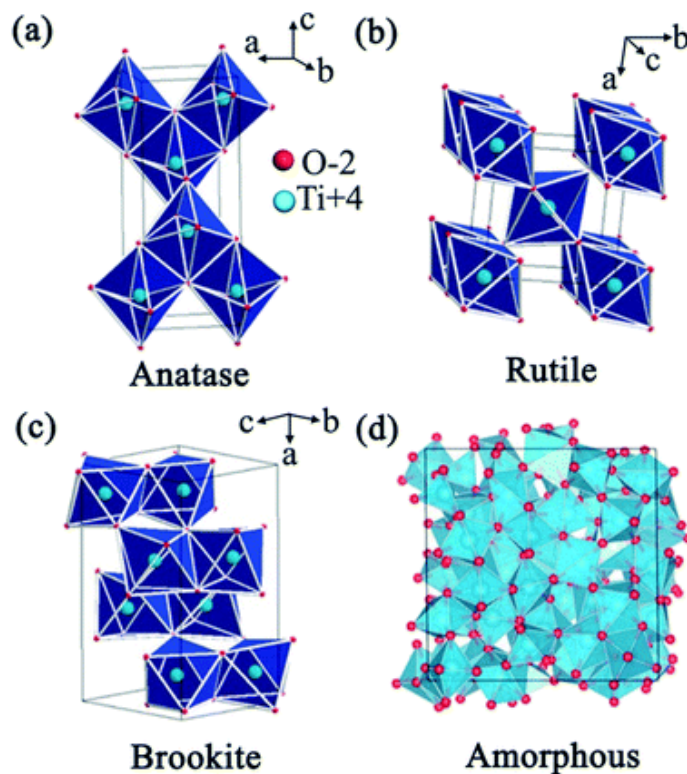

Figure 8 Anatase (a), rutile (b), brookite (c) and amorphous (d) phases of TiO_2 [30].

Optical properties of TiO_2

All four mentioned phases can exist in transparent form. In common applications TiO_2 is often regarded has having white colour and is added to paint as white pigment. In thin film applications TiO_2 films are usually transparent. Sometimes a yellow tint is reported, which is associated with oxygen vacancies [31]. Black TiO_2 has also been synthesised. The black colour is achieved by creating defects on the surface of the material [34]. In solar cell applications the transparent film is sought after.

The band gap of TiO_2 depends on the crystal structure of it. For rutile, the band gap is often reported to be around 3.0 eV and for the anatase phase around 3.2 eV [35]. Brookite has been reported to have a band gap of around 3.14 eV [29]. The amorphous phase of TiO_2 films exhibit a larger band gap of in a wider range: 3.4 – 3.47 eV [36]–[38] also 3.62 – 3.77 eV has been reported [39].

2.3.2 Depositing TiO_2 thin films

There are different methods of depositing TiO_2 thin films, including atomic layer deposition (ALD) [40], [41], pulsed laser deposition (PLD)　　　[35], hydrolysis [42], [43], sol-gel method [42], [44], chemical precipitation [45] and magnetron sputtering [30]. Some methods are suitable for thin film solar cells, and some are not. Depending on the method, controlling the substrate temperature is often critical to achieve a quality TiO_2 thin film. High temperatures however are not suitable for all absorber materials. For monograin layer CZTS solar cells high temperatures must be avoided mainly due to the incorporation of polymer compounds to fixate the monograins before TiO_2 deposition. A more thorough description of the monograin layer solar cell technology is seen in a later chapter. Radio frequency magnetron sputtering has been used to deposit a TiO_2 thin film on a CZTS has been conducted to show a dependency of band structure on the oxygen vacancies in TiO_2 [46]. On a CIGS solar cell TiO_2 has been deposited by the ALD method on the CdS buffer layer, to enable a smaller thickness of CdS layer. All parameters of the solar cell except the fill factor were increased with the application of a 15 nm TiO_2 layer [47] PLD also offers an appropriate method of TiO_2 thin film depositing. It has the advantage over ALD that it is much faster and does not require so precise control over the deposition parameters as ALD.

Pulsed laser deposition

Pulsed laser deposition is a versatile method of preparing a wide range of thin films. It works by the principle of irradiating a solid target of material with an extremely high energy density laser. The laser energy is transferred to the thermal energy of the

material fast, and the material is emitted from the target. The evaporated particles can be considered as ablation plasma, called plume. The evaporated material is transferred to the substrate. To ensure a clean path to the substrate and guarantee a stoichiometric thin film, PLD is usually conducted in a vacuum or controlled gas environment [35].
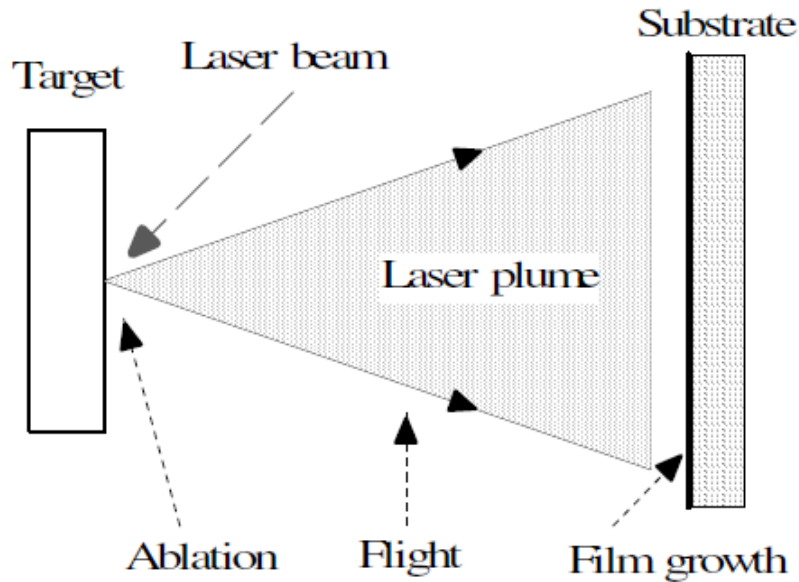

Figure 9 Fundamental process of PLD of a thin film [35].

The many advantages of PLD are that it can be used to deposit both low and high melting point materials, and also for non-sublimable materials. The deposition conditions can be tweaked to required values, and aforementioned stoichiometric result of the final thin film – it is mostly based on the target stoichiometry [35].

2.4 Summary of literature overview and aim of the thesis

An overview was given of the general working principles of a solar cell and why the development of a kesterite solar cell is beneficial – use of abundant materials. The kesterite solar cells suffer from a V_{OC} deficiency, which is mainly attributed to the interface recombinations in the p-n junction area. Some solutions to this deficiency involve depositing different buffer layers or interlayers (for example TiO_2) to introduce a "spike-like" conduction band offset in or near the p-n junction, which in turn may lead to reduced carrier recombination and thus increased V_{OC} of the solar cell. In this work TiO_2 was deposited as the alternate buffer layer or an intermediate layer by PLD method, which is in principle great for depositing thin layers of oxides. Following this the aim of the thesis is:

- To familiarise with the PLD deposition method and fabrication of monograin layer solar cells.

- To investigate the properties of the deposited TiO_2 thin films.

- To investigate the influence of the deposited TiO_2 thin films on the output parameters of the monograin layer solar cells:

  o In the structure of CZTS/TiO_2/CdS/i-ZnO/AZO to reduce the majority carrier recombination across the p-n junction.

  o In the structure of CZTS/CdS/TiO_2/AZO as the substitute of i-ZnO, in which the TiO_2 would act as a high resistance interlayer to prohibit shunting.

  o In the structure of CZTS/TiO_2/i-ZnO/AZO to see if a p-n junction of CZTS/TiO_2 could yield a beneficial effect.

3. EXPERIMENTAL

Classical thin film solar cells consist of different thin material layers that all work together to form a functional solar cell. Arguably the most important part of these layers is the absorber material, in which most of the solar light conversion to electricity is taking place. In a thin film technology solar cell, the absorber usually consists of a polycrystalline material deposited on a back contact. In a polycrystalline material the grain boundaries act as recombination centres of charge carriers. Additionally, the manufacturing of a large area chalcopyrite or kesterite absorber thin film is technically complicated, requiring vacuum technologies. Powder technologies offer an inexpensive and relatively simple method of producing small grains (mono crystals) of the absorber material. To achieve this, the initial precursor powders are recrystallized in a molten flux producing a powder with improved crystal structure. The advantages of the powder materials are that every grain will have a single-crystalline structure, doping impurities are uniformly distributed, the grains are similar in size [48].

3.1 Preparation of the MGL solar cell

The CZTS monograins were half-imbedded in a polymer material, usually an organic resin (epoxy). The resin is applied on a PET (polyethylene terephthalate) sheet, with which the organic resin has poor adhesion. The thickness of the organic resin (so the grains would not be entirely covered) was set by the doctor blade method – a bulk of resin was smoothly pushed over the PET sheet with a micrometre adjustable film applicator set to the desired height. The PET sheet was held in place by the vacuum table byko-drive XL, which also moved the film applicator. Before the imbedding process, the grains are generally covered with the buffer layer (CdS), but this can also be performed after the imbedding process.

The grains were treated in the resin until the end as in other thin film solar cell production. A high resistance oxide layer to decrease the probability of shunting and a transparent conductive layer, usually i-ZnO/AZO (aluminium doped zinc oxide, Al:ZnO) was added by radio frequency magnetron sputtering using the AJA International ATC 1200 device. In this work a TiO_2 layer was deposited by PLD, before the CdS deposition/on grains covered with CdS (instead of the *i*-ZnO) and instead of the CdS buffer layer. The PLD deposition parameters are introduced below. A collector electrode strip made of silver paste was applied on top of the transparent conductive oxide layer, which was later accessed by making a hole through the solar cell up to the silver paste. After applying the front electrode, the front side of the cell was ready, and it was fixed

against a glass piece by the same organic resin. The back contact was achieved by etching away the resin with concentrated H_2SO_4 and grinding the other half of the grains so they would be planar. Then graphite paste was added, which dries into a graphite contact, which will be the back contact. A simplified model of the reference solar cell (without the TiO_2) can be seen in Figure 10.
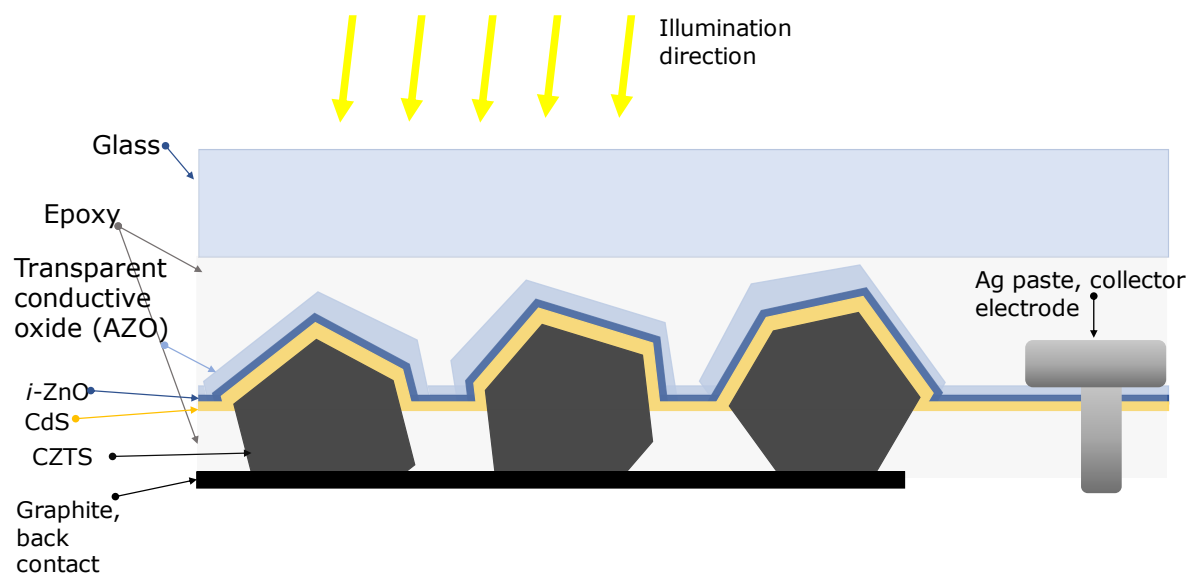

Figure 10 Simplified drawing of the monograin layer solar cell with the structure of graphite/CZTS/CdS/*i*-ZnO/AZO/Ag. Not to scale.

The monograin layer method combines the advantages of monocrystals with the advantages of polycrystalline technologies such as low cost and simple technology, possibility of flexible devices and using the material 100% [21].

3.2 Pulsed laser deposition of TiO₂ thin films

In this work, TiO_2 thin film was incorporated in the solar cell structure before, after and instead of the CdS buffer layer. The TiO_2 was deposited by PLD, and the target was a 2.5 cm hot-pressed pellet of 99.99% pure TiO_2 (Testbourne Inc.). Before inserting it to the deposition chamber, the target was manually grinded on P100 sandpaper and then cleaned with methanol. Before each deposition it was also pre-ablated to clean it from contaminants which may have deposited on the surface of the target when removing substrates from the chamber. The deposition was conducted by Neocera Pioneer 120 PLD system equipped with a 248 nm UV excimer laser (Compex). Pulse energy was approximately 200 mJ, and pulse repetition rate was 10 Hz. Deposition was conducted in vacuum chamber at 10^{-5} torr pressure. The target was rotated at 100°/sec and the substrate at 29°/sec. Target was also moved back and forth, so the laser spot would not hit only a certain radius on the target. The laser spot size was about 5 mm² and the

incident angle 45°. All depositions were conducted at room temperature (RT). Room temperature was chosen because of the organic resin used in making the monograin layer solar cell. Heating the resin up to 300° C [33], which is the transition temperature of am-TiO$_2$ to anatase phase, would degrade the resin and warp the solar cell shape. The pulse number was varied to achieve different thickness films. Number of pulses increases the deposition time, thus the longer the deposition time, the thicker the deposited film [49]. Altogether 5 different laser pulse numbers were used to achieve different thickness films of TiO$_2$ (450, 550, 1100, 2200 and 4400).

Figure 11 Pulsed laser deposition system Neocera Pioneer 120

The PLD processes were configured as follows: The depositions of TiO$_2$ for the CZTS/CdS/TiO$_2$/AZO solar cells were done separately. The deposition of TiO$_2$ for CZTS/TiO$_2$/*i*-ZnO/AZO and CZTS/TiO$_2$/CdS/*i*-ZnO/AZO were performed together during one process. The depositions for the Glass and polished Si/SiO$_2$ samples were performed separately from depositions on the solar cells. Depositions on the glass substrates were conducted to measure the transparency of the thin films. The depositions on the polished Si/SiO$_2$ were performed to measure the thickness and surface roughness of the thin films. Additionally, the composition of the thin films was measured, and Raman spectroscopy was conducted on the thin films deposited on the Si/SiO$_2$ substrates. The size of glass and Si/SiO2 samples was approximately 1 cm x 1cm. For comparison of solar cell output parameters another solar cell structure without TiO$_2$ was prepared – a reference sample with a structure of CZTS/CdS/*i*-ZnO/AZO as shown on Figure 10.

An overview of depositions can be seen in the Table 1 below.

Table 1 Overview of TiO$_2$ deposition substrates and the investigations of each test

PLD pulse numbers:	Solar cell structures			Glass 1cm x 1cm	Si/SiO$_2$ 1cm x 1cm
	CZTS/CdS/TiO$_2$...	CZTS/TiO$_2$...	CZTS/TiO$_2$/CdS...		
450	I-V measurements	I-V measurements	I-V measurements	UV-Vis	SEM
550	I-V measurements	I-V measurements	I-V measurements	UV-Vis	SEM
1100	I-V measurements	I-V measurements	I-V measurements	UV-Vis	SEM, Raman, AFM
2200	I-V measurements	I-V measurements	I-V measurements	UV-Vis	SEM
4400	I-V measurements	No samples left	I-V measurements	UV-Vis	SEM, XPS

3.3 Characterization methods used

3.3.1 Thickness and surface roughness measurements of TiO$_2$ film

Atomic force microscope (AFM)

In the first experiments the thickness and micromorphology of the deposited TiO2 thin films was tried to investigate by atomic force microscopy (AFM). The measurements were done with Bruker Multimode 8 AFM with a nanoscope V controller. Measurements were performed in peak-force tapping (scanasyst) mode using Scanasyst probes. Images were processed using Gwyddion and by applying a first-order polynomial line leveling, after which the image root-mean square roughness was extracted. The AFM analysis was performed by Dr. Peter Robert Walke at Tallinn University of Technology.

Scanning electron microscope (SEM)

High-resolution scanning electron microscope (HR-SEM) Zeiss ULTRA 55 was used for the study of morphology of obtained TiO_2 layers. The working principle of SEM is in detecting the weakly bound electrons of the material. The weakly bound electrons are kicked out of the material when the material is bombarded with and electron beam. These kicked out electrons are called secondary electrons. The secondary electrons are collected by a positively charged detector which sends a signal to a processing unit. An image of the surface is calculated and displayed based on the signal of the detector [50], [51]. To determine the film thickness the Si/SiO_2 substrates covered with TiO_2 thin film were broken and the thickness of the film was measured by SEM by looking at the cross-section of the TiO_2 covered Si/SiO_2 substrate. The SEM images were made by Dr. Valdek Mikli at Tallinn University of Technology.

3.3.2 Chemical composition and crystal structure

EDS Energy dispersive X-ray analysis (EDX)

Energy dispersive X-ray analysis is often performed during the SEM analysis of samples. During the electron beam interaction with the sample, characteristic X-rays are produced that are specific to each element, except for H and He. These characteristic X-rays are the basis of detecting the elemental composition of the material using a energy dispersive X-ray spectrometer [51]. The intensity of the detected signal is proportional to the concentration of the element in the sample. This method is not very accurate and requires an experienced and knowledgeable operator to use it effectively but is good for quick analysis if SEM is used anyways. In this work Zeiss FEG-SEM Ultra-55 scanning electron microscope was used with Bruker Esprit 1.8 system. The EDX measurements were carried out by Dr. Valdek Mikli at Tallinn University of Technology.

Room Temperature Micro-Raman spectroscopy

Raman spectroscopy is a common non-destructive analysis method in solid state physics. The working principle of Raman spectroscopy is non-elastic scattering of monochromatic light off the sample. The non-elastic scattering is caused by the interaction of the monochromatic light with the object's molecules and the vibration modes of the sample crystals [52]. Raman spectroscopy enables the analysis of the sample's crystal structure and from that the chemical composition and crystallinity.

For that Horiba's LabRam HR 800 spectrometer with a multichannel CCD detection system in the backscattering configuration using a 532 nm laser line with the spot size of 5 μm was used. The Raman measurements were carried out by the help of Dr. Reelika Kaupmees at Tallinn University of Technology.

X-ray photoelectron spectroscopy (XPS)

X-Ray photoelectron spectroscopy is another method for measuring the elemental composition of a material. It works by radiating the material of interest with X-rays, which in turn induces the emission of electrons from the material. This is called the photoelectric effect. The kinetic energy of these electrons is measured and knowing the energy of initial X-rays, the binding energy of the electrons can be calculated. For each element, the electron binding energies are of some specific values (band of values). These values have been mapped in databases, with which the obtained spectra are compared to. This is the basis for obtaining the elemental composition by the XPS method [53]. In this work Kratos Analytical Axis Ultra DLD spectrometer was used. The XPS measurements were carried out by Dr. Mati Danilson at Tallinn University of Technology.

3.3.3 Optical properties

UV-Vis-NIR spectroscopy

Measuring the optical properties of a material in the ultraviolet (UV) (wavelengths 190-400 nm), visible (Vis) (400-800 nm) and near infrared (NIR) (780-2500 nm) ranges. By this method it is possible to directly measure how large part of incident light goes through (is transmitted), reflects and is absorbed by the material. In this work the transmittance was measured in the visible and ultraviolet range. To measure transmittance the intensity of incident light and the light that transmitted the material are compared at each wavelength. These transmittance values are plotted against the wavelength and a spectrum is achieved [54]. Based on this spectrum it is possible to calculate the band gap of the material. This is achieved by transforming the transmittance value at each measured point into the absorption coefficient (Equation 3.1) and then creating a Tauc plot based on these coefficients. By extending the linear part of the Tauc plot to the x-axis (x-axis is the photon energy value of light wavelengths), the band gap energy will be revealed.

Calculating the absorption coefficient:

$$\alpha = \frac{\ln\left(\frac{100}{T}\right)}{t}$$

Equation 3.1

Where, α – coefficient of absorption.

T – thin film transmittance at a given wavelength (%).

t – thickness of thin film (nm).

The thickness values were obtained by SEM as mentioned previously. The device used for UV-Vis analysis was Agilent Technologies Cary series 5000 UV-Vis-NIR spectroscope. The transmittance measurements were performed with the help of Dr. Olga Volobujeva at Tallinn University of Technology.

3.3.4 Measurements of solar cell output parameters

The measuring of the monograin layer solar cell output parameters was conducted with Keithley 2400 SourceMeter in conjunction with a Newport solar light simulator, which is in accordance with AAA class conditions and matches the AM 1.5 solar radiation spectrally and by intensity 100 mW/cm^2. The measurement error in V_{oc} values can be considered up to 10 mV.

Series and shunt resistances

To find the series and shunt resistances the measured current and voltage values of the solar cells under no illumination were fitted by the Equation 3.2– a modified version of Equation 2.1. As the value of I - measured current (A), is on both sides of the equation, then the equation was solved numerically by trial of each unknown in the equation until the mean root square difference of the calculated current value from the measured current value at each measured V value was as low as possible. For this Excel solver was used. Example of a fitted curve by this method can be seen on Figure 12.

$$I = I_0 \cdot \left(e^{\frac{(V - I \cdot R_S)}{nkT}} - 1\right) + \frac{V - I \cdot R_S}{R_{Sh}}$$

Equation 3.2

Where: I - measured current (A)
I_{Ph} – light generated current (A)
I_0 – saturation current (A)
V – Voltage value (V)

R_S – Series resistance (Ω)

n – ideality factor

k – Boltzmann constant (W·s/K)

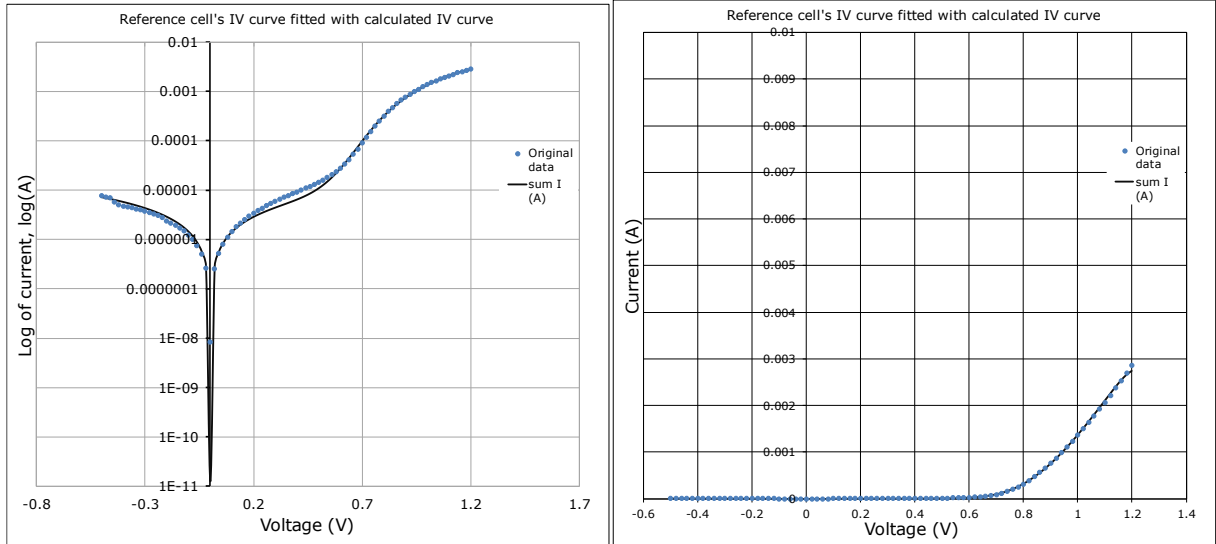T – temperature (K)

R_{Sh} – Shunt resistance (Ω)

Figure 12 Fitted IV-curve of the reference cell's (CZTS/CdS/*i*-ZnO/AZO) best measurement on the right and in logarithmic scale on the left.

4. RESULTS AND DISCUSSION

4.1 Properties of the deposited TiO2 thin films

4.1.1 Structural and elemental study of deposited TiO2 thin films

The Raman spectroscopy method was used for structural characterization of TiO2 thin films prepared by pulsed laser deposition. The Raman spectroscopy was to confirm that the deposited layer is amorphous as the depositions were performed at a lower temperature (<300° C) than required to achieve a crystalline structure, as previously mentioned. Amorphous TiO_2 should not have any phonon modes to provide a peak in the Raman spectroscopy. On the Figure 13 it can be seen, this was the case and existence of amorphous TiO2 was confirmed – no TiO_2 crystalline phase peaks were seen (604 cm^{-1}, 438 cm^{-1} and 231cm^{-1} for rutile and 636 cm^{-1}, 516 cm^{-1}, 395 cm^{-1}, 143 cm^{-1} for the anatase phase) [55]. The peaks seen on Figure 13 at 521 cm^{-1} and 302 cm^{-1} can be attributed to the Si/SiO_2 substrate [56], [57].
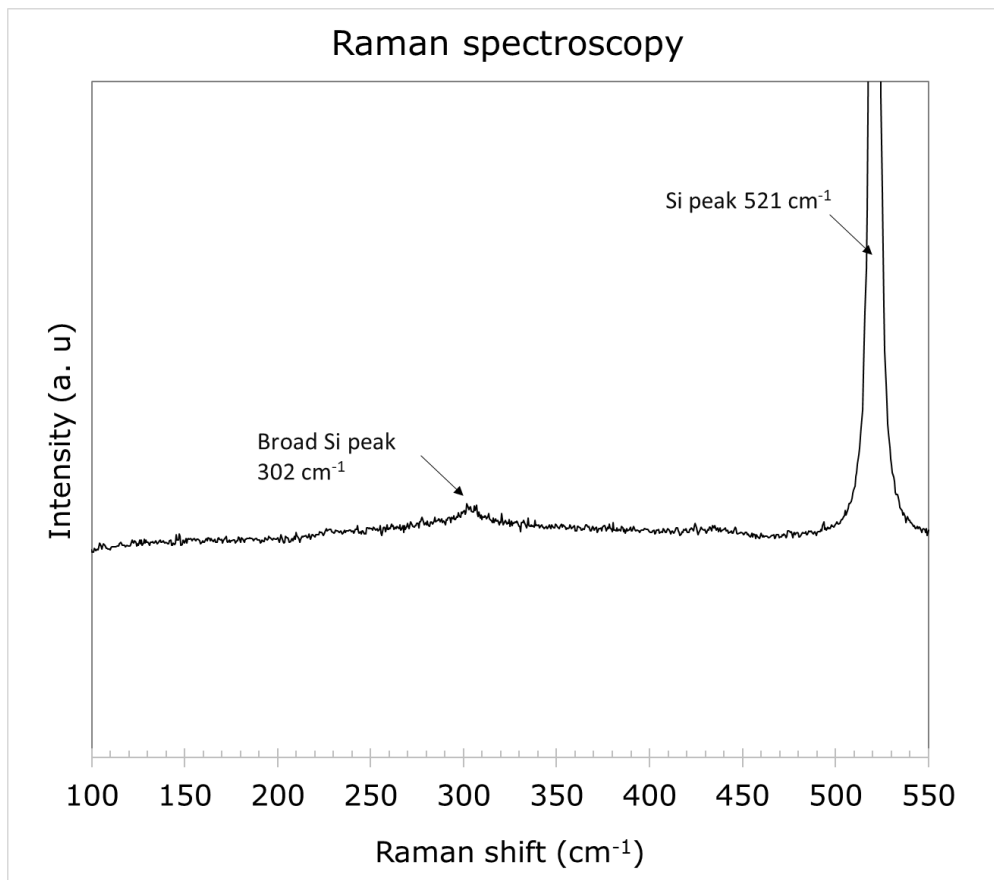

Figure 13 Raman spectra of amorphous TiO_2 film on Si/SiO_2 substrate.

In addition, an EDX analysis of the surface of the TiO_2 was conducted to confirm that a TiO_2 layer truly existed on the Si/SiO$_2$ sample. On Figure 14 the EDX pattern can be seen, confirming the existence of both elemental Ti and O signals in the deposited layers. The Si peak originates from the substrate, as the EDX analysis depth is deeper than the thickness of the TiO_2 layer.
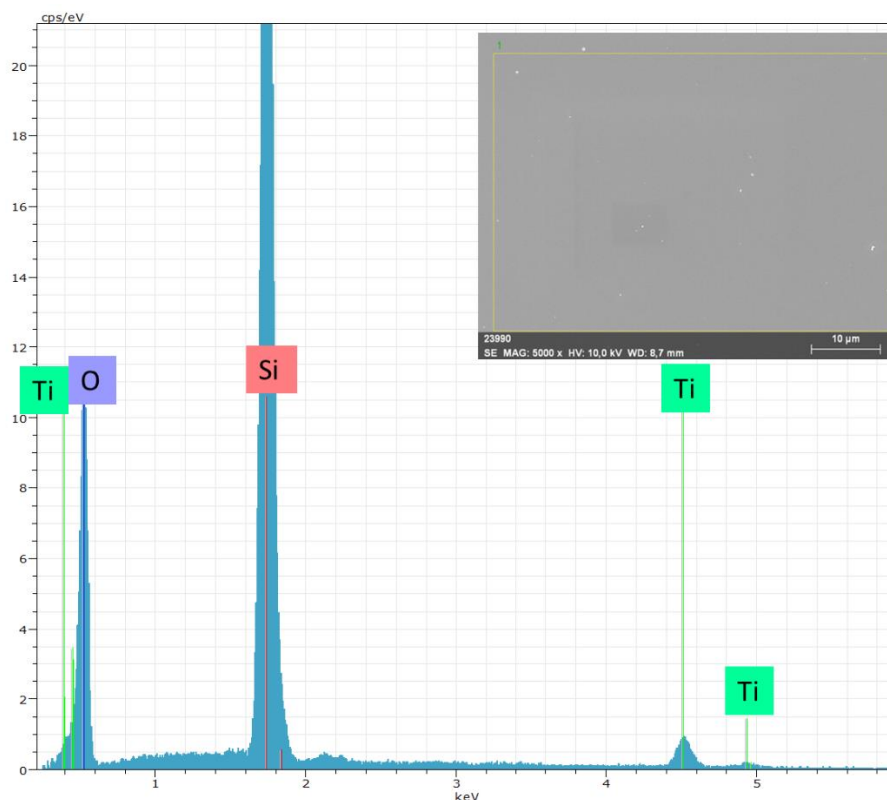

Figure 14 Energy-dispersive X-ray spectrum of TiO2 thin layer. Inset image shows the analyzed area.

The X-ray photoelectron spectroscopy (XPS) showed a confirmation of TiO_2 existence. The analysis was performed on a Si/SiO$_2$ sample with TiO_2 thickness of approximately 49 nm. The Ti 2p core-level peaks at 464.3 eV and 458.6 eV [58], [59] correspond with the TiO_2 and core-level peaks at 462.9 eV and 457.0 eV are associated with the existence of Ti^{3+} atoms, indicating some oxygen vacancies [59]. The O 1s core-level peak at 530 eV is associated with TiO_2 [58], [59] and the 531 eV peak is associated with -OH bonds, indicating either some minor contamination or adsorbed water in the material. The data was also confirmed by cross-checking with NIST X-ray Photoelectron Spectroscopy Database, Version 4.1 (National Institute of Standards and Technology, Gaithersburg, 2012) [60].
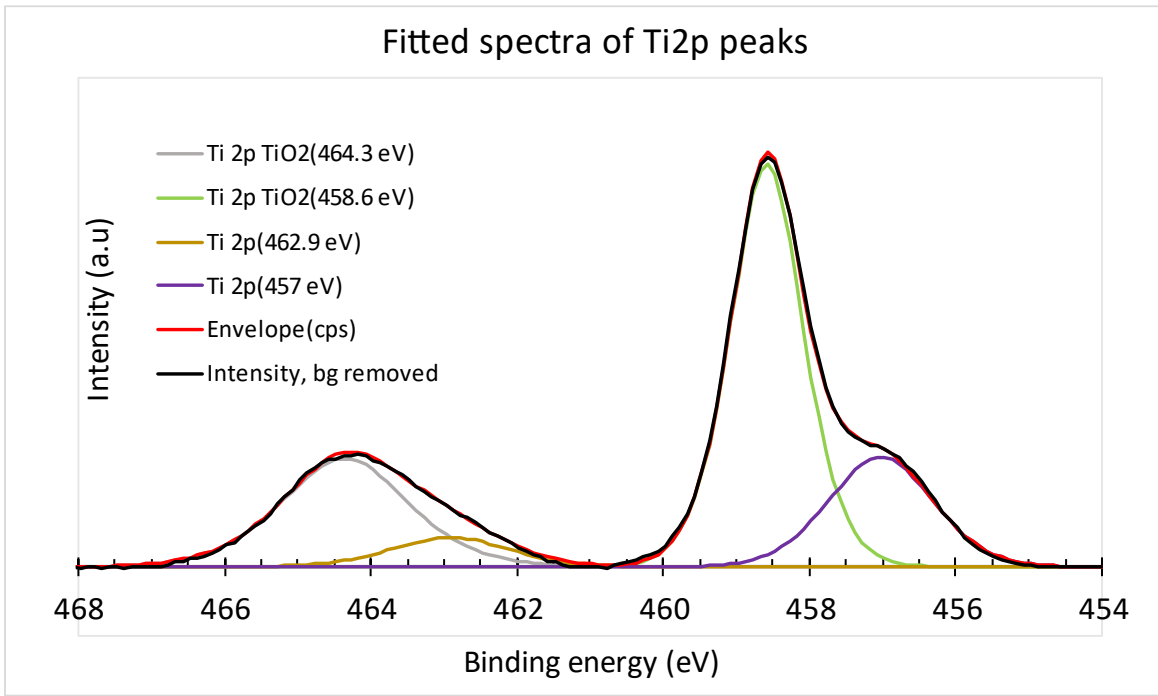
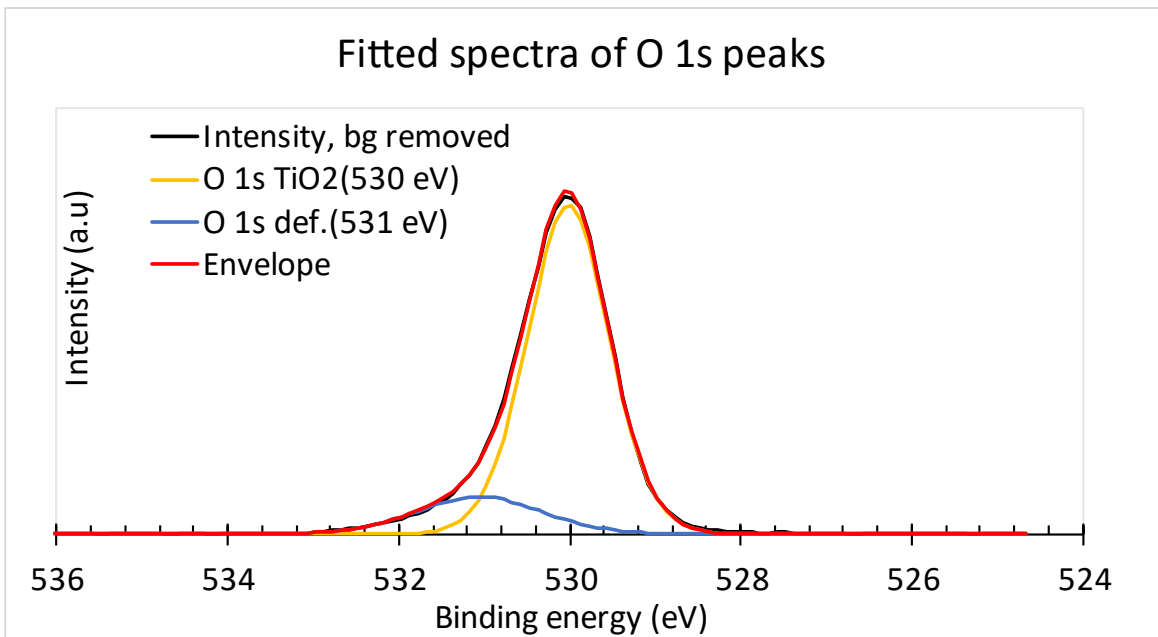Figure 15 Fitted XPS spectra of 49 nm thick TiO_2, Ti 2p core-level peaks.

Figure 16 Fitted XPS spectra of 49 nm thick TiO_2, O 1s core-level peaks.

4.1.2 Morphology and film thickness of deposited TiO₂ thin film

At first an attempt was made to measure the thickness of the deposited TiO_2 films by atomic force microscopy (AFM) by measuring the height difference between a covered and uncovered area on the polished Si/SiO_2 substrate covered with TiO_2 thin film. It is suspected that the transition from the area of Si substrate covered by TiO_2 and not covered was smooth and that is why the edge was not found and measurement could not me made by AFM. A surface roughness measurement was also conducted. The surface analysis revealed that with 1100 laser pulses, the surface roughnesses of the TiO_2 and SiO_2 layers were 0.31 nm and 0.35 nm, respectively. It can be concluded from the results that the deposited TiO_2 films have a smooth surface. AFM surface images of Si/SiO_2 and TiO_2 thin film deposited on the Si/SiO_2 layer are shown in Figure 17.
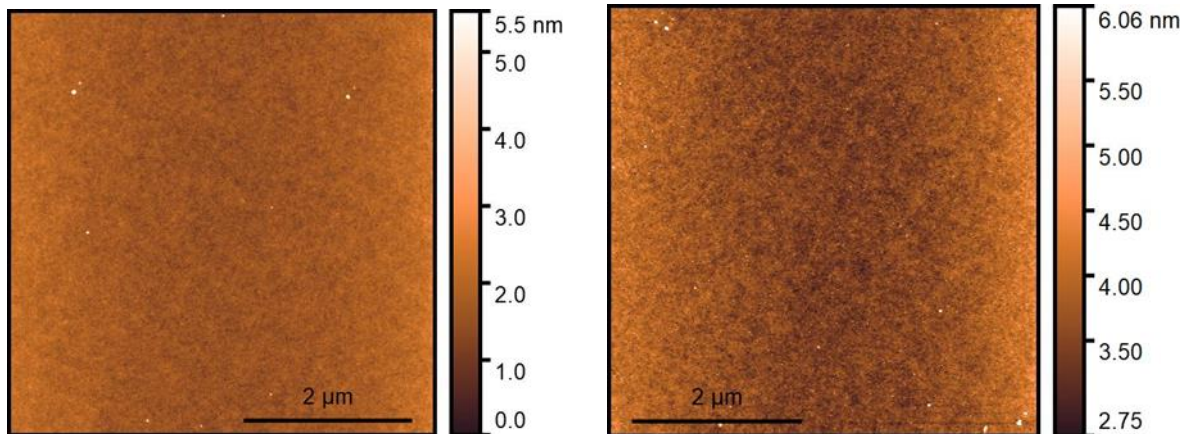

Figure 17 AFM surface images of Si/SiO_2 (left image) and TiO_2 thin layers (right image). Since it was not possible to determine the thickness of the deposited TiO_2 films with the AFM method, it was decided to measure the thicknesses by SEM as previously mentioned. In the Figure 18, the number of laser pulses and the thickness of the corresponding TiO_2 layer has been shown. (Near data points the values used for graph are shown – top value is pulse numbers and lower value the thickness of corresponding TiO_2 layer). A linear growth of the TiO_2 layer thickness can be approximated from these values.
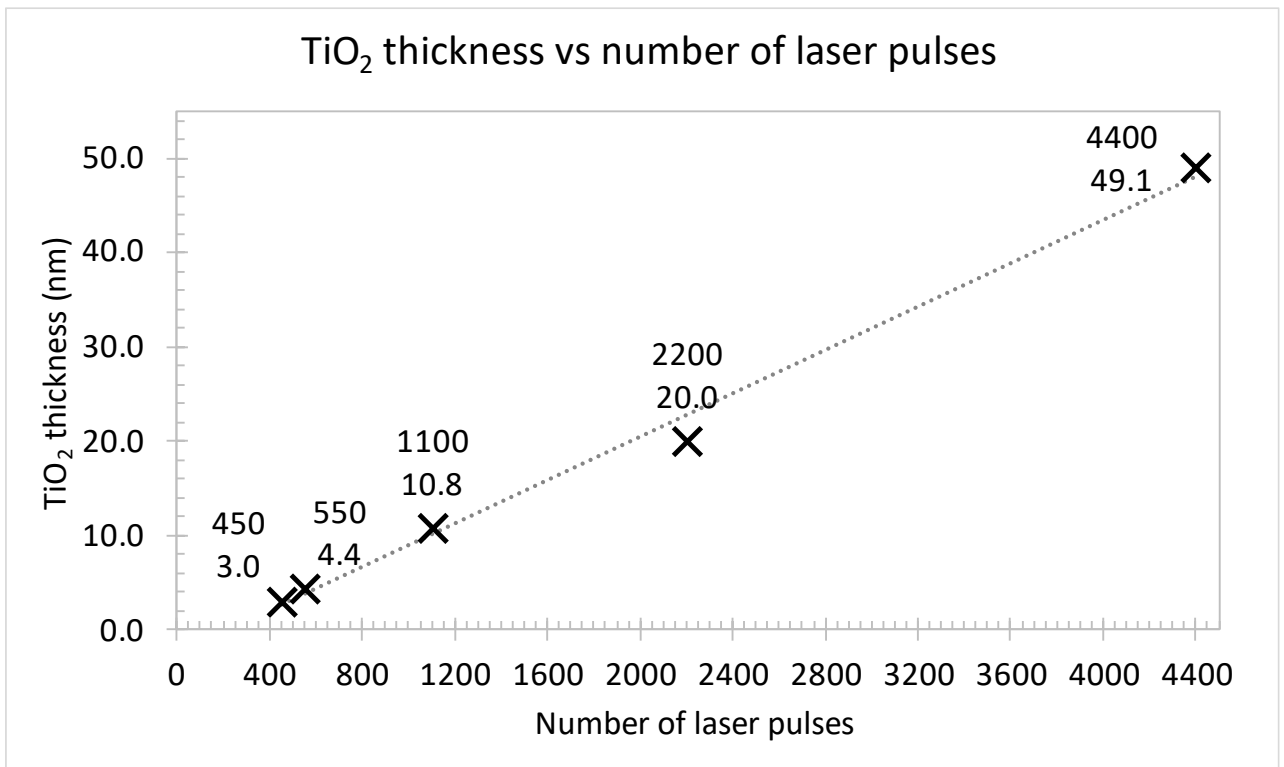
Figure 18 TiO₂ thickness measured by SEM, compared with the number of laser pulses. The top number at each point signifies the pulse numbers and the lower number signifies the average measured thickness of the corresponding TiO₂ film.

As the measurements of thickness were approximate, in further text and graphs, the thicknesses are referenced as such 3 nm; 4 to 5 nm; 10 to 11 nm; 20 nm; 48 to 49 nm according to the order of the deposition pulse numbers (450, 550, 1100, 2200 4400).
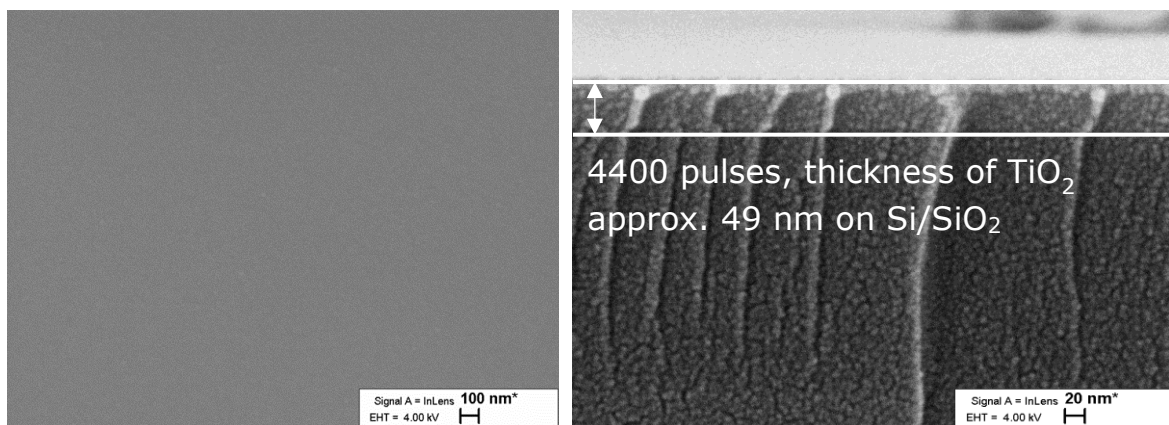

Figure 19 Surface of TiO₂ on Si/SiO₂ (left). Example of SEM measurement of the thickness of the TiO₂ layer(right).

4.1.3 Optical properties of deposited TiO$_2$ thin film

The transparency of the TiO$_2$ films deposited on the glass substrates was analyzed in the UV-Vis region. The results of the measurement can be seen below on Figure 20. The measurement indicates that the transparency decreases with the increase of the thin film thickness. It can also be seen that the higher thickness layers lose transparency faster with the decrease of the wavelength of light from 400 nm to 320 nm. This can be attributed to the larger absorption of light at these wavelengths, as the energy of this light is approaching the theoretical band gap of TiO$_2$, indicating increased absorption of light.
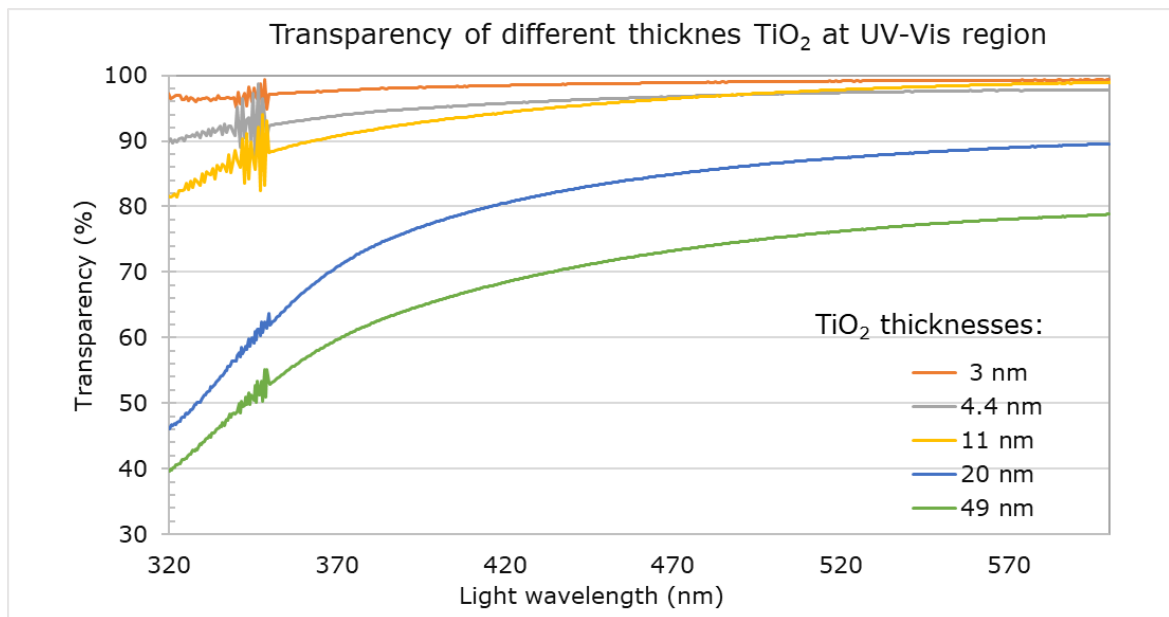

Figure 20 Different thickness TiO$_2$ layers and their corresponding transparency at given wavelengths.

The optical band gaps of deposited TiO$_2$ thin films were determined from the transmittance spectra. The absorption coefficient was found by the Equation 3.1. The 49 nm thick TiO$_2$ layer was chosen to show the value of the band gap, as the thickness of the layer is the highest. Having a high thickness layer, means that the photons of the sufficient energy have a higher probability of exciting an electron from the valence band to the conduction band (absorbing). This in turn gives a larger difference in the absorption coefficient value for low and high energy photons, providing a larger part of the linear area in the Tauc plot, Figure 21. Extending the linear area to the x-axis gives the band gap value, which was determined to be approximately 3.4eV, coinciding with literature [36]–[38]
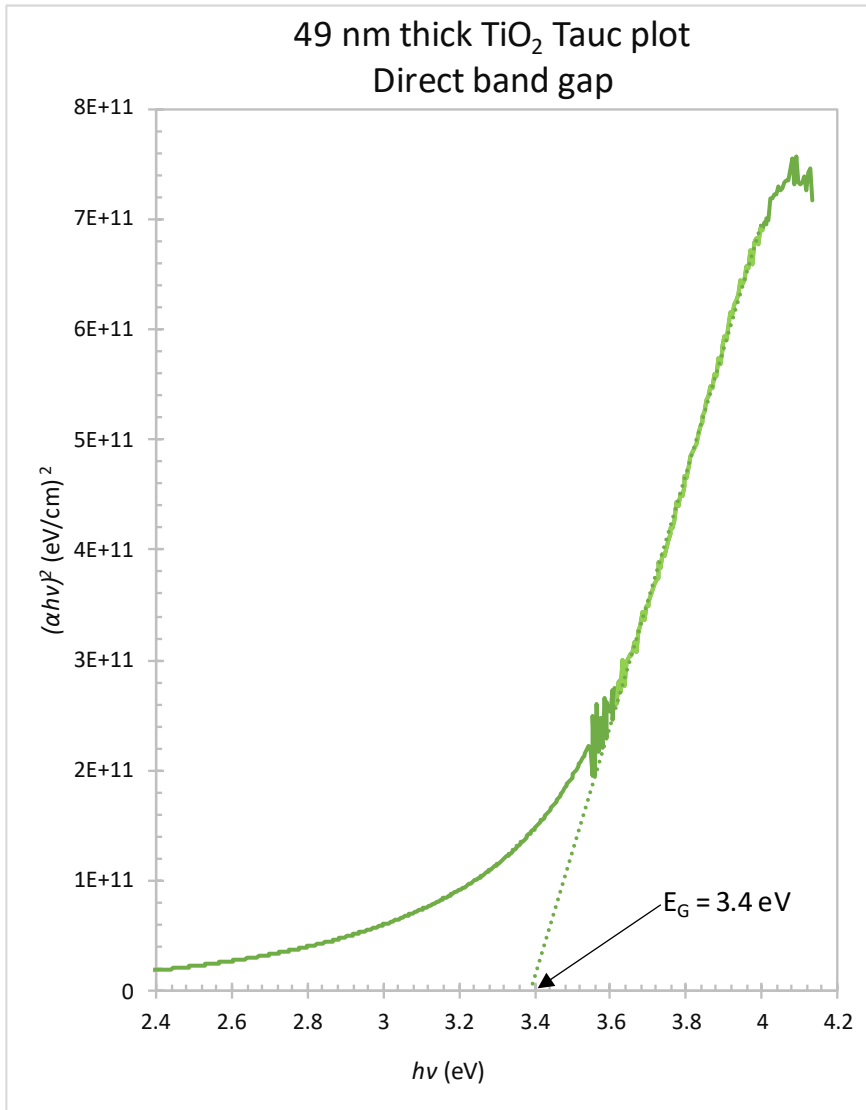
Figure 21 Tauc plot of the 49 nm thick TiO$_2$ thin film. Band gap value can be seen.

4.2 Characterization of MGL solar cells

The monograin solar cell parameters were measured and the influence of PLD deposited TiO$_2$ thin layer on the solar cell parameters for the different type of structures mentioned previously are shown in next chapters.

4.2.1 Characterization of CZTS/TiO$_2$/CdS/i-ZnO/AZO structure solar cells

The CZTS/TiO$_2$/CdS/i-ZnO/AZO structure solar cell parameters were measured and can be seen of Figure 22. The CZTS/TiO$_2$/CdS/i-ZnO/AZO solar cells' output parameters were all decreased compared to the reference cell. The reasons for these results of the CZTS/TiO$_2$/CdS/i-ZnO/AZO solar cells may be that the TiO$_2$ does not form a good enough

buffer layer with CZTS and the TiO_2 layer before the CdS layer is not as suitable for the p-n junction formation as previously thought. It may also be possible that in CZTS/TiO_2/CdS/i-ZnO/AZO solar cells there is no protection for the absorber material during the PLD process, high velocity TiO_2 particles damage the absorber surface. Thus, instead of reducing interface recombinations, the PLD of TiO_2 instead increases the recombinations.
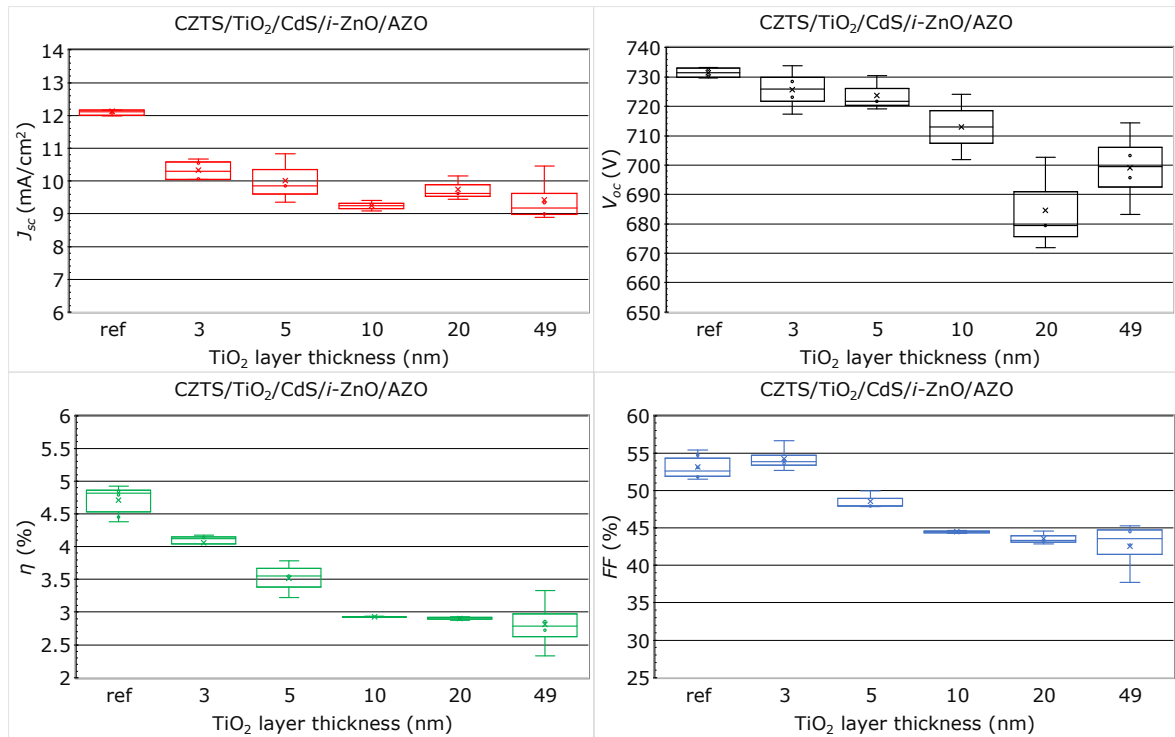

Figure 22 The output parameters of the CZTS/TiO_2/CdS/i-ZnO/AZO structure solar cells depending on the thickness of the TiO_2 layer.

The series and shunt resistances of the CZTS/TiO_2/CdS/i-ZnO/AZO solar cells can be seen on Figure 23. It can be seen that the series resistance of the solar cells initially increases with the increase of TiO_2 layer thickness up to 10 nm. A sudden decrease in series resistance is seen in solar cells with 20 nm and 49 nm thickness TiO_2 layers. The shunt resistances are all relatively close in terms of order of magnitude (from 10^3 to 10^4).
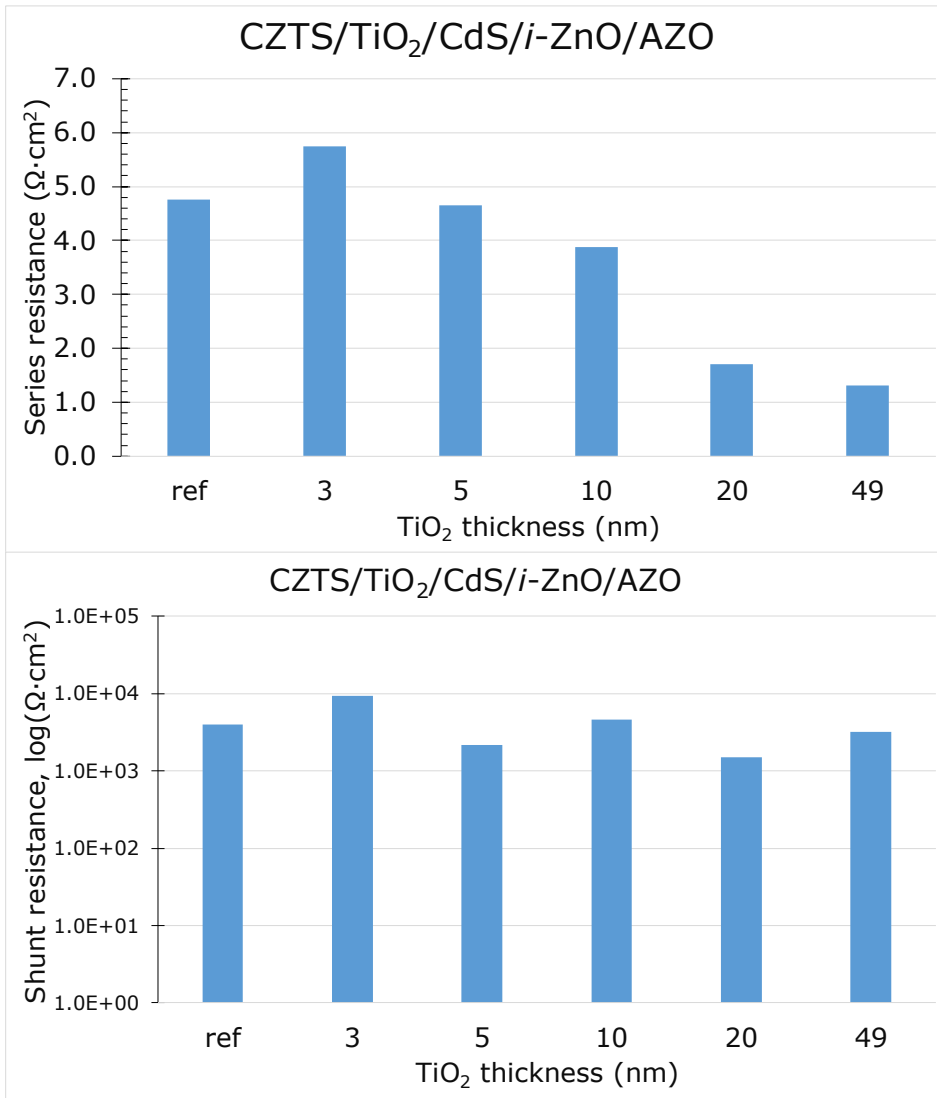
Figure 23 The calculated series resistance value (top) and shunt resistance value (bottom) of the CZTS/TiO$_2$/CdS/i-ZnO/AZO solar cells depending on the thickness of TiO$_2$ layer. The best performing measurement point of each solar cell was chosen for this.

4.2.2 Characterization of CZTS/CdS/TiO$_2$/AZO structure solar cells

The CZTS/CdS/TiO$_2$/AZO structure solar cell parameters were measured and can be seen on Figure 24. A stable V_{OC} increase of $\approx$ 18 mV was seen only for the CZTS/CdS/TiO$_2$/AZO structure solar cells, in the other solar cells rather the opposite effect was seen. In the CZTS/CdS/TiO$_2$/AZO structure, the other output parameters of the solar cells were very close to the reference cell. It is possible the slight increase in V_{OC} can be attributed to the increase in shunt resistance shown on Figure 25 lower graph. Increase in shunt resistance may be attributed to the higher resistivity of TiO$_2$ when compared to ZnO.
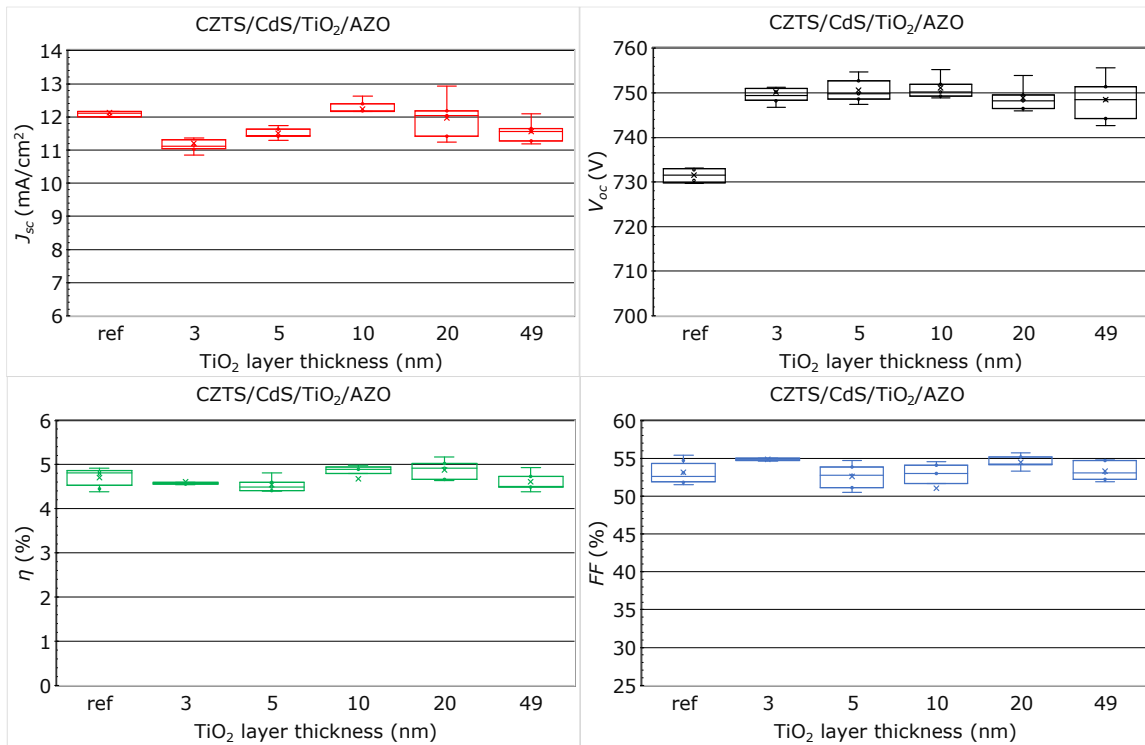
Figure 24 The output parameters of the CZTS/CdS/TiO$_2$/AZO structure solar cells depending on the thickness of the TiO$_2$ layer.

The series (top) and shunt resistances (lower) of the CZTS/CdS/TiO$_2$/AZO solar cells can be seen on Figure 25. As mentioned, an increase in the shunt resistances of the solar cells was evident when compared to the reference cell (from order of magnitude of 10^3 (ref) to 10^5-10^6). This may be the cause of the slight improvement in the V_{OC} value. An increase in the series resistance was also seen for all solar cells with this structure. Again, the series resistance increased with the increase of TiO$_2$ layer thickness until 5 nm. Then the resistance value started reducing with the TiO$_2$ layer thickness.

Figure 25 The calculated series resistance value (top) and shunt resistance value (bottom) of the CZTS/CdS/TiO$_2$/AZO solar cells depending on the thickness of TiO$_2$ layer. The best performing measurement point of each solar cell was chosen for this.

4.2.3 Characterization of CZTS/TiO$_2$/*i*-ZnO/AZO structure solar cells

The solar cells with the structure of CZTS/TiO$_2$/*i*-ZnO/AZO output parameters (Figure 26) were all lower than the reference cell as was the case with CZTS/TiO$_2$/CdS/*i*-ZnO/AZO solar cells' output parameters. Again, this may be due to no CdS layer protecting the absorber material during the PLD process. It is also probable that the amorphous TiO$_2$ is not as suitable for the p-n junction formation as CdS is.
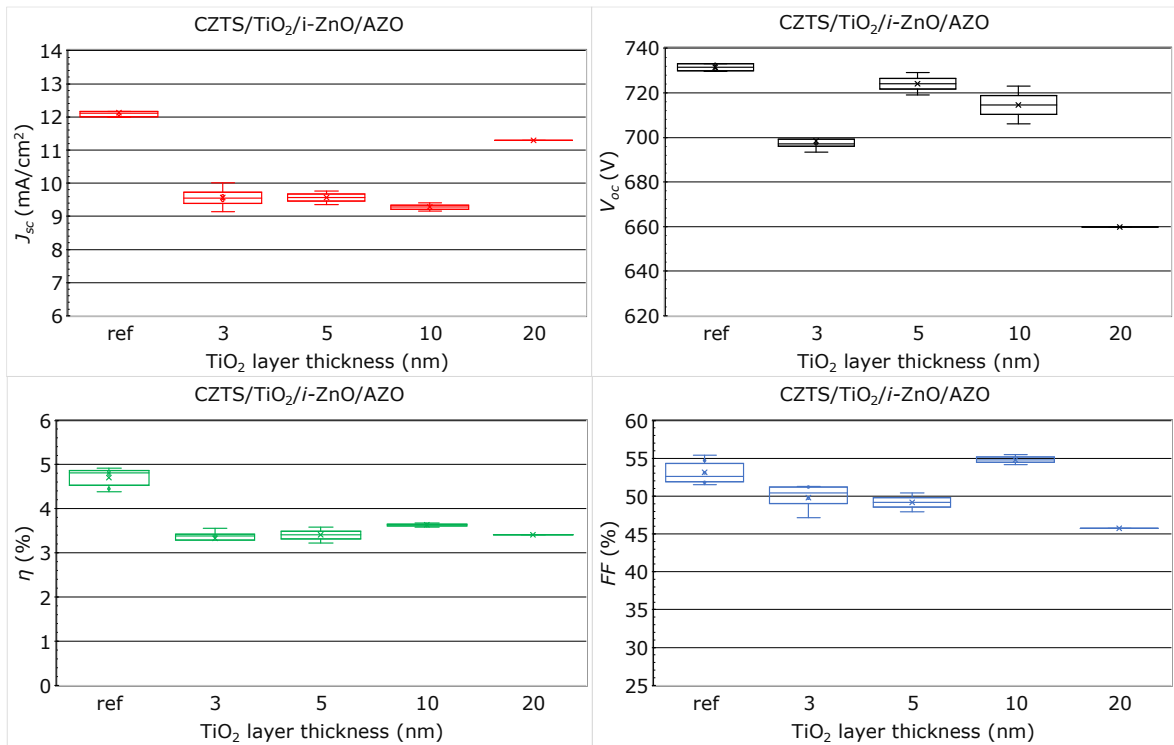
Figure 26 The output parameters of the CZTS/TiO$_2$/i-ZnO/AZO structure solar cells depending on the thickness of the TiO$_2$ layer.

The series (top) and shunt resistances (lower) of the CZTS/TiO$_2$/i-ZnO/AZO solar cells can be seen on Figure 27. Similarly, to the CZTS/TiO$_2$/CdS/i-ZnO/AZO solar cells, the shunt resistances of the solar cells are within the same order of magnitude (10^3 to 10^4). Curiously the series resistance value at 5 nm thickness of TiO$_2$ was the highest, being twice higher than the values for solar cells with 10 nm and 20 nm thickness TiO$_2$ layer.
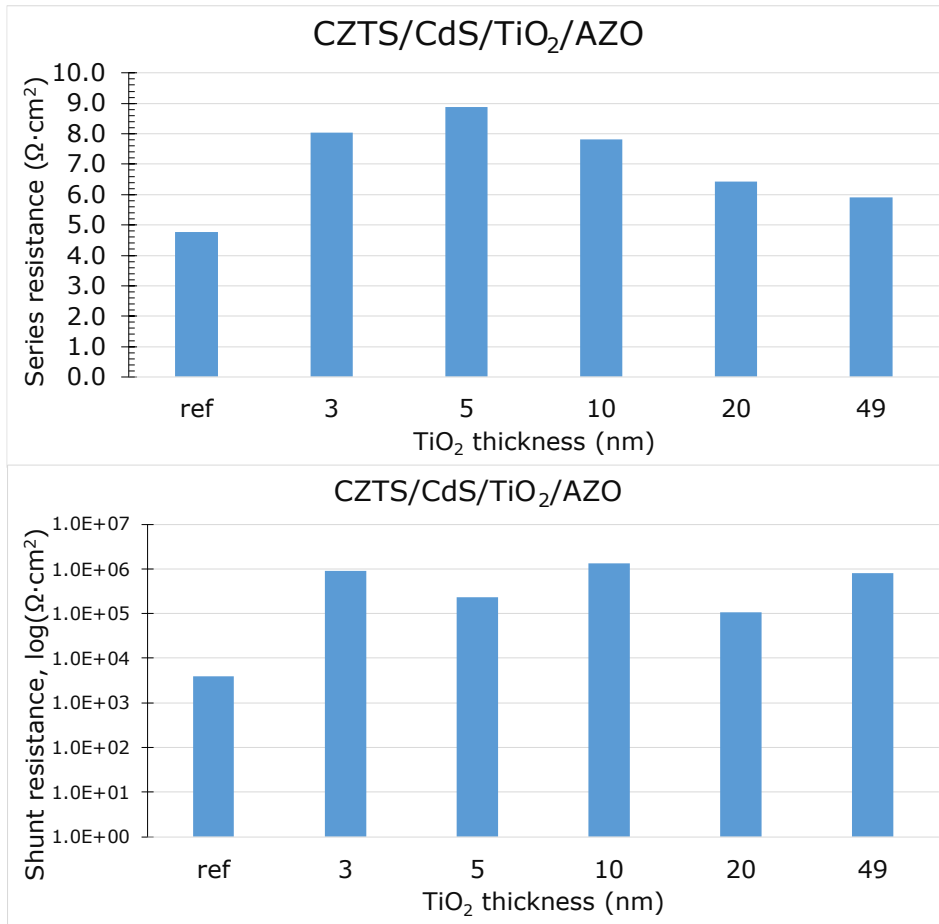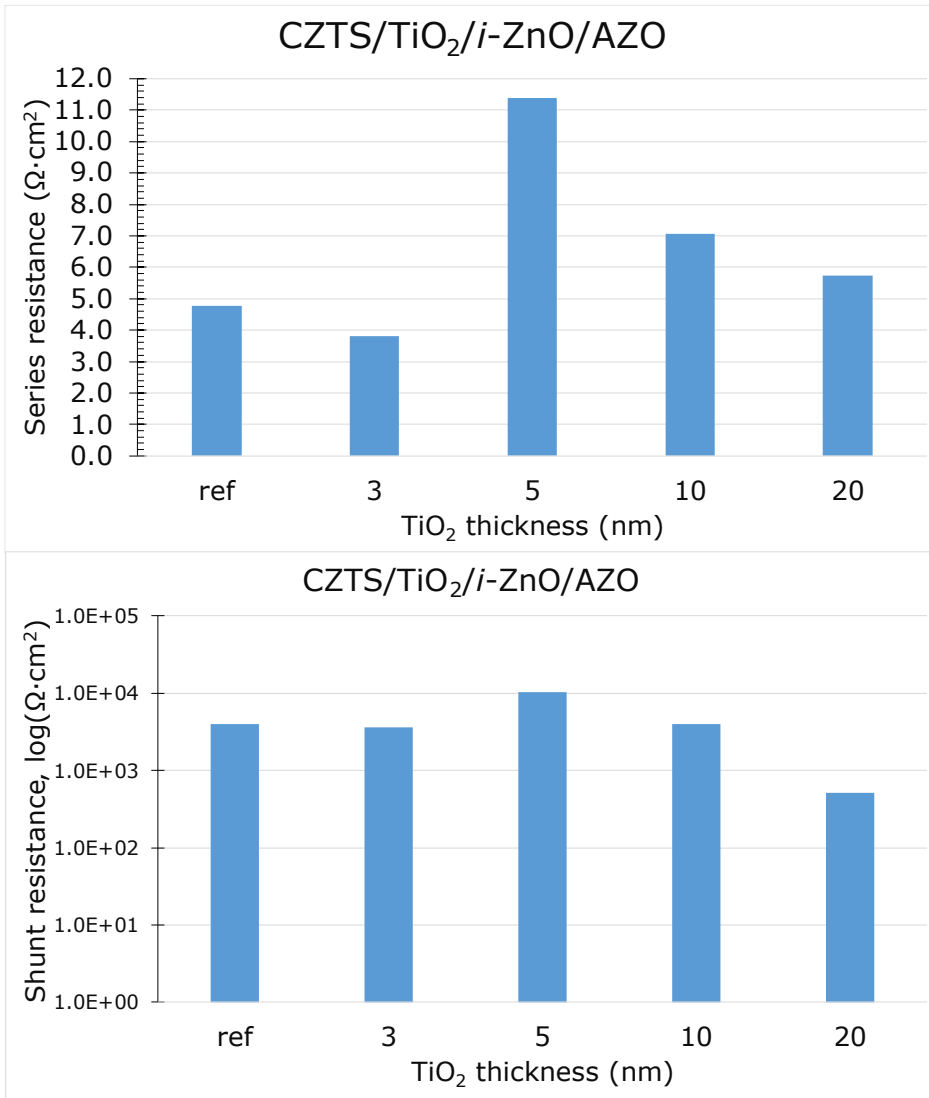
Figure 27 The calculated series resistance value (top) and shunt resistance value (bottom) of the CZTS/TiO$_2$/i-ZnO/AZO solar cells depending on the thickness of TiO$_2$ layer. The best performing measurement point of each solar cell was chosen for this.

CONCLUSIONS

In this work the effect of different thickness (from 3 to 49 nm) pulsed laser deposited amorphous thin film TiO_2 on the output parameters of the CZTS solar cells was investigated. In addition, the morphology and optical properties of TiO_2 thin films were characterized.

The amorphous structure of deposited TiO_2 layers was confirmed by the Raman spectroscopy. The thicknesses of the TiO_2 layers increased with the deposition time linearly. AFM analysis revealed that the deposited films are smooth having a low surface roughness. The transparencies of the TiO_2 layers varied with the thickness in the visible region from near 100% transparency for 3 nm thick layer to around 80% transparency for the 49 nm thick layer. The deposited TiO_2 thin layers exhibited an optical band gap of 3,4 eV. The XPS study of the TiO_2 thin layer confirmed the existence of TiO_2 but also indicated that the thin film contained some oxygen vacancies.

The TiO_2 thin films were deposited in 3 different solar cell structures: CZTS/TiO_2/CdS/i-ZnO/AZO, CZTS/CdS/TiO_2/AZO and CZTS/TiO_2/i-ZnO/AZO, with the aim of reducing interface recombinations of the solar cells and through that the V_{OC} of the solar cell.

The effect of TiO_2 layer on the photovoltaic parameters of CZTS/TiO_2/CdS/i-ZnO/AZO and CZTS/TiO_2/i-ZnO/AZO solar cells was negative. This may be due to formation of additional recombination centres at the interface CZTS/TiO_2 during PLD process.

The effect of the TiO_2 layer on the PV parameters of CZTS/CdS/TiO_2/AZO was mildly positive. A slight stable increase in the V_{OC} of the solar cells was seen, the other parameters of the solar cells were similar to the reference cell regardless of the TiO_2 layer thickness. Shunt resistance increase (from a magnitude of 10^3 (ref) to 10^5-10^6 $\Omega \cdot cm^2$) was also observed for these solar cells when compared to the reference cell. This may indicate that the TiO_2 acted as a more effective high resistance intermediate layer in the solar cell than i-ZnO.

SUMMARY

In the current global climate and political environment, it is becoming an increasing reality that drastic actions must be taken to achieve both the green energy targets and energy independency. In achieving this new solar cell technologies could help immensely by being technologically capable to be incorporated to buildings, devices, vehicles, etc. Among those technologies are the (Cu_2ZnSnS_4) CZTS solar cells. They employ abundant materials and can be incorporated into flexible and integrated solar cell solutions. The champion CZTS solar cell has an efficiency of 14.1%, which is yet too low for commercial solutions. A major problem of the CZTS based solar cells is the interface recombination, which limits the open-circuit voltage (V_{OC}) of the solar cell. Solutions to reduce the recombination include incorporating an intermediate layer in the solar cell structure (or replacing the buffer layer, with a more suitable one).

This thesis focused on the deposition of TiO_2 by the pulsed laser deposition method and characterizing of the achieved thin film and seeing its effect in different 3 different locations in the CZTS monograin layer solar cell. The solar cell structures were as follows: CZTS/TiO_2/CdS/*i*-ZnO/AZO, CZTS/CdS/TiO_2/AZO and CZTS/TiO_2/*i*-ZnO/AZO.

The achieved TiO_2 thin films were smooth and amorphous, as the depositions were conducted under 300° C, which is required for crystallisation into the anatase phase. Low temperature depositions were required due to the restrictions of the monograin layer solar cell including an organic resin, which is temperature sensitive. The phase of the thin film was confirmed by Raman spectroscopy, where no characteristic modes of crystalline TiO_2 were seen. The thin films had a band gap of 3.4 eV, which agrees with the literature for the amorphous phase TiO_2. Oxygen vacancies were detected in the thin film by X-ray photoelectron spectroscopy.

The effect of TiO_2 layer on the CZTS/TiO_2/CdS/*i*-ZnO/AZO and CZTS/TiO_2/*i*-ZnO/AZO solar cells was negative. All the output parameters of the solar cells were lowered compared to the reference. This may be because there is no protection for the absorber material during the PLD process, high velocity TiO_2 particles damage the absorber surface. Thus, instead of reducing interface recombinations, the PLD of TiO_2 instead increases the recombinations.

The effect of the TiO_2 layer on the CZTS/CdS/TiO_2/AZO was mildly positive. A slight increase in the V_{OC} of the solar cells was seen, the other parameters of the solar cells were similar to the reference cell regardless of the TiO_2 layer thickness. Shunt resistance increase (from a magnitude of 10^3 (ref) to 10^5-10^6 $\Omega \cdot cm^2$) was also observed for these

solar cells when compared to the reference cell. This may indicate that the TiO_2 acted as a more effective high resistance intermediate layer in the solar cell than i-ZnO.

Regarding these results, it can be said that the achieved thin films of TiO_2 were successfully characterised, but the incorporation into the CZTS monograin layer solar cells was not beneficial. The negative effects of the TiO_2 in the solar cell structure may indicate the unsuitability of the TiO_2 as the material to reduce recombinations, or the unsuitability of the depositing method of TiO_2. Although the amorphous and anatase phase of TiO_2 have similar electrical properties, in general it is often true that the crystalline material has better electrical properties than the amorphous phase of the same material.

In the future the incorporation of intermediate layers in the CZTS monograin layer solar cells should not be disregarded, but an investigation of a different suitable material (ZnSnO, ZnCdS, etc.) should maybe be pursued. A different low temperature deposition method may also be tried to include the TiO_2 layer in the solar cell.

LIST OF REFERENCES

[1]   *World Energy Transitions Outlook 2022: 1.5°C Pathway*. International Renewable Energy Agency, 2022. [Online]. Available: www.irena.org

[2]   K. Ranabhat, L. Patrikeev, A. Antal'evna-Revina, K. Andrianov, V. Lapshinsky, and E. Sofronova, "An introduction to solar cell technology," *Istrazivanja i projektovanja za privredu*, vol. 14, no. 4, pp. 481–491, 2016, doi: 10.5937/jaes14-10879.

[3]   L. Yin, G. Cheng, Y. Feng, Z. Li, C. Yang, and X. Xiao, "Limitation factors for the performance of kesterite Cu_2ZnSnS_4 thin film solar cells studied by defect characterization," *RSC Adv*, vol. 5, no. 50, pp. 40369–40374, 2015, doi: 10.1039/C5RA00069F.

[4]   K. Sun *et al.*, "Over 9% Efficient Kesterite Cu_2ZnSnS_4 Solar Cell Fabricated by Using $Zn_{1-x}Cd_xS$ Buffer Layer," *Adv Energy Mater*, vol. 6, no. 12, p. 1600046, Jun. 2016, doi: 10.1002/aenm.201600046.

[5]   C. Platzer-Björkman *et al.*, "Reduced interface recombination in Cu_2ZnSnS_4 solar cells with atomic layer deposition $Zn_{1-x}Sn_xO_y$ buffer layers," *Appl Phys Lett*, vol. 107, no. 24, p. 243904, Dec. 2015, doi: 10.1063/1.4937998.

[6]   M. Bär *et al.*, "Cliff-like conduction band offset and KCN-induced recombination barrier enhancement at the CdS/Cu_2ZnSnS_4 thin-film solar cell heterojunction," *Appl Phys Lett*, vol. 99, no. 22, p. 222105, Nov. 2011, doi: 10.1063/1.3663327.

[7]   Nisika *et al.*, "Energy level alignment and nanoscale investigation of a-TiO_2/Cu-Zn-Sn-S interface for alternative electron transport layer in earth abundant Cu-Zn-Sn-S solar cells," *J Appl Phys*, vol. 126, no. 19, p. 193104, Nov. 2019, doi: 10.1063/1.5121874.

[8]   H. Bencherif, L. Dehimi, N. Mahsar, E. Kouriche, and F. Pezzimenti, "Modeling and optimization of CZTS kesterite solar cells using TiO2 as efficient electron transport layer," *Materials Science and Engineering: B*, vol. 276, p. 115574, Feb. 2022, doi: 10.1016/j.mseb.2021.115574.

[9]   K. Mertens, *Photovoltaics: Fundamentals, Technology, and Practice*. Wiley, 2018.

[10]   A. Reinders, P. Verlinden, W. van Sark, and A. Freundlich, *Photovoltaic solar energy: from fundamentals to applications*. John Wiley & Sons, Ltd, 2017.

[11]   NREL, "Best research-cell efficiency chart," *https://www.nrel.gov/pv/assets/pdfs/best-research-cell-efficiencies-rev220630.pdf*, 2022. NREL.gov (accessed Oct. 31, 2022).

[12]   V. Pakštas *et al.*, "Improvement of CZTSSe film quality and superstrate solar cell performance through optimized post-deposition annealing," *Sci Rep*, vol. 12, no. 1, p. 16170, Sep. 2022, doi: 10.1038/s41598-022-20670-1.

[13]   S. Chen, J.-H. Yang, X. G. Gong, A. Walsh, and S.-H. Wei, "Intrinsic point defects and complexes in the quaternary kesterite semiconductor Cu_2ZnSnS_4," *Phys Rev B*, vol. 81, no. 24, p. 245204, Jun. 2010, doi: 10.1103/PhysRevB.81.245204.

[14]   J. Zhou *et al.*, "A precisely regulating phase evolution strategy for highly efficient kesterite solar cells," 2022, doi: https://doi.org/10.48550/arXiv.2210.13714.

[15]   B. Shin, O. Gunawan, Y. Zhu, N. A. Bojarczuk, S. J. Chey, and S. Guha, "Thin film solar cell with 8.4% power conversion efficiency using an earth-abundant Cu_2ZnSnS_4 absorber," *Progress in Photovoltaics: Research and Applications*, vol. 21, no. 1, pp. 72–76, Jan. 2013, doi: 10.1002/pip.1174.

[16]   T. Gokmen, O. Gunawan, T. K. Todorov, and D. B. Mitzi, "Band tailing and efficiency limitation in kesterite solar cells," *Appl Phys Lett*, vol. 103, no. 10, p. 103506, Sep. 2013, doi: 10.1063/1.4820250.

[17]   C. J. Hages, N. J. Carter, and R. Agrawal, "Generalized quantum efficiency analysis for non-ideal solar cells: Case of $Cu_2ZnSnSe_4$," *J Appl Phys*, vol. 119, no. 1, p. 014505, Jan. 2016, doi: 10.1063/1.4939487.

[18]   A. Santoni, F. Biccari, C. Malerba, M. Valentini, R. Chierchia, and A. Mittiga, "Valence band offset at the CdS/Cu_2ZnSnS_4 interface probed by x-ray

photoelectron spectroscopy," *J Phys D Appl Phys*, vol. 46, no. 17, p. 175101, May 2013, doi: 10.1088/0022-3727/46/17/175101.

[19] C. Tamin, D. Chaumont, O. Heintz, and M. Adnane, "Estimation of band alignment at CdS/Cu$_2$ZnSnS$_4$ hetero-interface by direct XPS measurements," *Surface and Interface Analysis*, vol. 52, no. 12, pp. 985–990, Dec. 2020, doi: 10.1002/sia.6881.

[20] S. Rondiya *et al.*, "CZTS/CdS: interface properties and band alignment study towards photovoltaic applications," *Journal of Materials Science: Materials in Electronics*, vol. 29, no. 5, pp. 4201–4210, Mar. 2018, doi: 10.1007/s10854-017-8365-5.

[21] E. Ghorbani, "On efficiency of earth-abundant chalcogenide photovoltaic materials buffered with CdS: the limiting effect of band alignment," *Journal of Physics: Energy*, vol. 2, no. 2, p. 025002, Apr. 2020, doi: 10.1088/2515-7655/ab6942.

[22] T. Minemoto *et al.*, "Theoretical analysis of the effect of conduction band offset of window/CIS layers on performance of CIS solar cells using device simulation," *Solar Energy Materials and Solar Cells*, vol. 67, no. 1–4, pp. 83–88, Mar. 2001, doi: 10.1016/S0927-0248(00)00266-X.

[23] W.-C. Chen *et al.*, "Interface engineering of CdS/CZTSSe heterojunctions for enhancing the Cu$_2$ZnSn(S,Se)$_4$ solar cell efficiency," *Mater Today Energy*, vol. 13, pp. 256–266, Sep. 2019, doi: 10.1016/j.mtener.2019.05.015.

[24] A. Guchhait *et al.*, "Enhancement of Open-Circuit Voltage of Solution-Processed Cu$_2$ZnSnS$_4$ Solar Cells with 7.2% Efficiency by Incorporation of Silver," *ACS Energy Lett*, vol. 1, no. 6, pp. 1256–1261, Dec. 2016, doi: 10.1021/acsenergylett.6b00509.

[25] M. Gansukh *et al.*, "Energy band alignment at the heterointerface between CdS and Ag-alloyed CZTS," *Sci Rep*, vol. 10, no. 1, p. 18388, Oct. 2020, doi: 10.1038/s41598-020-73828-0.

[26] Y.-F. Qi *et al.*, "Engineering of interface band bending and defects elimination via a Ag-graded active layer for efficient (Cu,Ag)$_2$ZnSn(S,Se)$_4$ solar cells," *Energy Environ Sci*, vol. 10, no. 11, pp. 2401–2410, Nov. 2017, doi: 10.1039/C7EE01405H.

[27] S. Tajima, M. Umehara, and T. Mise, "Photovoltaic properties of Cu$_2$ZnSnS$_4$ cells fabricated using ZnSnO and ZnSnO/CdS buffer layers," *Jpn J Appl Phys*, vol. 55, no. 11, p. 112302, Nov. 2016, doi: 10.7567/JJAP.55.112302.

[28] H. Sun *et al.*, "Efficiency Enhancement of Kesterite Cu$_2$ZnSnS$_4$ Solar Cells via Solution-Processed Ultrathin Tin Oxide Intermediate Layer at Absorber/Buffer Interface," *ACS Appl Energy Mater*, vol. 1, no. 1, pp. 154–160, Jan. 2018, doi: 10.1021/acsaem.7b00044.

[29] L. Stephen, "Titanium Dioxide Versatile Solid Crystalline: An Overview," in *Assorted Dimensional Reconfigurable Materials*, IntechOpen, 2020. doi: 10.5772/intechopen.92056.

[30] S. Sun, P. Song, J. Cui, and S. Liang, "Amorphous TiO$_2$ nanostructures: synthesis, fundamental properties and photocatalytic applications," *Catal Sci Technol*, vol. 9, no. 16, pp. 4198–4215, 2019, doi: 10.1039/C9CY01020C.

[31] I. Ali, M. Suhail, Z. A. Alothman, and A. Alwarthan, "Recent advances in syntheses, properties and applications of TiO$_2$ nanostructures," *RSC Adv*, vol. 8, no. 53, pp. 30125–30147, 2018, doi: 10.1039/C8RA06517A.

[32] B. Prasai, B. Cai, M. K. Underwood, J. P. Lewis, and D. A. Drabold, "Properties of amorphous and crystalline titanium dioxide from first principles," *J Mater Sci*, vol. 47, no. 21, pp. 7515–7521, Nov. 2012, doi: 10.1007/s10853-012-6439-6.

[33] W. S. Shih, S. J. Young, L. W. Ji, W. Water, and H. W. Shiu, "TiO$_2$-Based Thin Film Transistors with Amorphous and Anatase Channel Layer," *J Electrochem Soc*, vol. 158, no. 6, p. H609, 2011, doi: 10.1149/1.3561271.

[34] T. S. Rajaraman, S. P. Parikh, and V. G. Gandhi, "Black TiO$_2$: A review of its properties and conflicting trends," *Chemical Engineering Journal*, vol. 389, p. 123918, Jun. 2020, doi: 10.1016/j.cej.2019.123918.

[35] S. Kitazawa, S. Yamamoto, and J. C. Taylor, "Preparation of functional TiO_2 films by pulsed laser deposition on proper substrates," in *Advances in chemistry research*, vol. 4, Nova Science, 2010, p. 333.

[36] Y. Ju, L. Li, Z. Wu, and Y. Jiang, "Effect of Oxygen Partial Pressure on the Optical Property of Amorphous Titanium Oxide Thin Films," *Energy Procedia*, vol. 12, pp. 450–455, 2011, doi: 10.1016/j.egypro.2011.10.060.

[37] S. ben Amor, L. Guedri, G. Baud, M. Jacquet, and M. Ghedira, "Influence of the temperature on the properties of sputtered titanium oxide films," 2002.

[38] E. Gofuku, Y. Toyoda, Y. Uehara, M. Kohara, and M. Nunoshita, "Highly conductive TiO_2 thin films prepared by EB-modification," *Appl Surf Sci*, vol. 48–49, pp. 343–350, Jan. 1991, doi: 10.1016/0169-4332(91)90355-N.

[39] S. B. Amor, L. Guedri, G. Baud, M. Jacquet, and M. Ghedira, "Influence of the temperature on the properties of sputtered titanium oxide films," *Mater Chem Phys*, vol. 77, no. 3, pp. 903–911, Jan. 2003, doi: 10.1016/S0254-0584(02)00189-X.

[40] C. Ban *et al.*, "Atomic layer deposition of amorphous TiO_2 on graphene as an anode for Li-ion batteries," *Nanotechnology*, vol. 24, no. 42, p. 424002, Oct. 2013, doi: 10.1088/0957-4484/24/42/424002.

[41] M. Hannula, H. Ali-Löytty, K. Lahtonen, E. Sarlin, J. Saari, and M. Valden, "Improved Stability of Atomic Layer Deposited Amorphous TiO_2 Photoelectrode Coatings by Thermally Induced Oxygen Defects," *Chemistry of Materials*, vol. 30, no. 4, pp. 1199–1208, Feb. 2018, doi: 10.1021/acs.chemmater.7b02938.

[42] S. Lee, K. Lee, W. D. Kim, S. Lee, D. J. Shin, and D. C. Lee, "Thin Amorphous TiO_2 Shell on CdSe Nanocrystal Quantum Dots Enhances Photocatalysis of Hydrogen Evolution from Water," *The Journal of Physical Chemistry C*, vol. 118, no. 41, pp. 23627–23634, Oct. 2014, doi: 10.1021/jp508315m.

[43] D. Su, S. Dou, and G. Wang, "Anatase TiO_2: Better Anode Material Than Amorphous and Rutile Phases of TiO_2 for Na-Ion Batteries," *Chemistry of Materials*, vol. 27, no. 17, pp. 6022–6029, Sep. 2015, doi: 10.1021/acs.chemmater.5b02348.

[44] G. Wu *et al.*, "Amorphous titanium oxide passivated lithium titanium phosphate electrode for high stable aqueous lithium ion batteries with oxygen tolerance," *Electrochim Acta*, vol. 246, pp. 720–729, Aug. 2017, doi: 10.1016/j.electacta.2017.06.093.

[45] B. Liu *et al.*, "Influence of dimensionality and crystallization on visible-light hydrogen production of Au@TiO_2 core-shell photocatalysts based on localized surface plasmon resonance," *Catal Sci Technol*, vol. 8, no. 4, pp. 1094–1103, 2018, doi: 10.1039/c7cy02083j.

[46] Nisika, K. Kaur, M. K. Yadav, A. Bag, and M. Kumar, "Suppression of interfacial oxygen vacancies for efficient charge extraction at CZTS/TiO_2 heterojunction," *Appl Phys Lett*, vol. 118, no. 4, p. 041601, Jan. 2021, doi: 10.1063/5.0038458.

[47] J. Löckinger *et al.*, "TiO_2 as intermediate buffer layer in Cu(In,Ga)Se_2 solar cells," *Solar Energy Materials and Solar Cells*, vol. 174, pp. 397–404, Jan. 2018, doi: 10.1016/j.solmat.2017.09.030.

[48] M. Altosaar *et al.*, "Monograin layer solar cells," *Thin Solid Films*, vol. 431–432, pp. 466–469, May 2003, doi: 10.1016/S0040-6090(03)00167-6.

[49] A. Mohamed Salih, "The Influence of the Number of Laser Pulses on the Thickness and Roughness of TiO_2 Thin Films Fabricated Using Pulsed Laser Deposition," *American Journal of Polymer Science and Technology*, vol. 5, no. 1, p. 29, 2019, doi: 10.11648/j.ajpst.20190501.14.

[50] K. H. Buschow and S. Jürgen Cahn, Robert W. Flemings, Merton C. Ilschner, Bernhard Kramer, Edward J. Mahajan, "Scanning Electron Microscopy," in *Encyclopedia of Materials - Science and Technology*, Elsevier., 2001. [Online]. Available: https://app.knovel.com/hotlink/pdf/id:kt00B7APH1/encyclopedia-materials/scanning-electron-microscopy

[51] J. I. Goldstein *et al.*, *Scanning Electron Microscopy and X-Ray Microanalysis*, 4th ed. 2017.

[52] M. Schumm, "ZnO-based semiconductors studied by Raman spectroscopy: semimagnetic alloying, doping, and nanostructures.," *Doctoral dissertation*, 2008.

[53] J. Kumar, "Photoelectron Spectroscopy: Fundamental Principles and Applications," in *Handbook of Materials Characterization*, Cham: Springer International Publishing, 2018, pp. 435–495. doi: 10.1007/978-3-319-92955-2_12.

[54] S. N. Jha, "6.1 Ultraviolet and Visual Spectroscopy," in *Rapid Detection of Food Adulterants and Contaminants - Theory and Practice*, Elsevier, 2016. [Online]. Available: https://app.knovel.com/hotlink/pdf/id:kt010WKXZ2/rapid-detection-food/ultraviolet-visual-spectroscopy

[55] M. Lubas, J. J. Jasinski, M. Sitarz, L. Kurpaska, P. Podsiad, and J. Jasinski, "Raman spectroscopy of TiO_2 thin films formed by hybrid treatment for biomedical applications," *Spectrochim Acta A Mol Biomol Spectrosc*, vol. 133, pp. 867–871, Dec. 2014, doi: 10.1016/j.saa.2014.05.045.

[56] S. Lebedkin, C. Blum, N. Stürzl, F. Hennrich, and M. M. Kappes, "A low-wavenumber-extended confocal Raman microscope with very high laser excitation line discrimination," *Review of Scientific Instruments*, vol. 82, no. 1, p. 013705, Jan. 2011, doi: 10.1063/1.3520137.

[57] V. Mankad, S. K. Gupta, P. K. Jha, N. N. Ovsyuk, and G. A. Kachurin, "Low-frequency Raman scattering from Si/Ge nanocrystals in different matrixes caused by acoustic phonon quantization," *J Appl Phys*, vol. 112, no. 5, p. 054318, Sep. 2012, doi: 10.1063/1.4747933.

[58] T. Eleutério, S. Sério, O. M. N. D. Teodoro, N. Bundaleski, and H. C. Vasconcelos, "XPS and FTIR Studies of DC Reactive Magnetron Sputtered TiO_2 Thin Films on Natural Based-Cellulose Fibers," *Coatings*, vol. 10, no. 3, p. 287, Mar. 2020, doi: 10.3390/coatings10030287.

[59] Tamara Potlog, Petru Dumitriu, Marius Dobromir, and Dumitru Luca, "XRD and XPS Analysis of TiO_2 Thin Films Annealed in Different Environments," *Journal of Materials Science and Engineering B*, vol. 4, no. 6, Jun. 2014, doi: 10.17265/2161-6221/2014.06.004.

[60] A. v. Naumkin, A. Kraut-Vass, S. W. Gaarenstroom, and C. J. Powell, "NIST X-ray Photoelectron Spectroscopy Database, Version 4.1," *National Institute of Standards and Technology (NIST)*, 2012. http://srdata.nist.gov/xps/ (accessed Jan. 02, 2023).